# UC San Diego

## UC San Diego Electronic Theses and Dissertations

**Title**

Electrodynamic Shaker Capability Estimation Through Experimental Dynamic Substructuring

**Permalink**

https://escholarship.org/uc/item/3qh6q6nt

**Author**

Fickenwirth, Peter Hans

**Publication Date**

2023

Peer reviewed|Thesis/dissertation

eScholarship.org Powered by the California Digital Library
University of California

UNIVERSITY OF CALIFORNIA SAN DIEGO

# Electrodynamic Shaker Capability Estimation Through Experimental Dynamic Substructuring

A thesis submitted in partial satisfaction of the requirements
for the degree of Master of Science

in

Structural Engineering with Specialization in Structural Health Monitoring and Non-Destructive Evaluation

by

Peter Hans Fickenwirth

Committee in charge:

Michael D. Todd, Chair
Charles R. Farrar
Dustin Y. Harvey
John F. Schultze
Qiang Zhu

2023

Copyright

Peter Hans Fickenwirth, 2023
All rights reserved.

The thesis of Peter Hans Fickenwirth is approved, and it is acceptable in quality and form for publication on microfilm and electronically.

University of California San Diego
2023

# TABLE OF CONTENTS

**THESIS APPROVAL PAGE** ..... **iii**

**TABLE OF CONTENTS** ..... **iv**

**LIST OF ABBREVIATIONS** ..... **vi**

**LIST OF SYMBOLS** ..... **vii**

**LIST OF FIGURES** ..... **ix**

**LIST OF TABLES** ..... **xii**

**ACKNOWLEDGEMENTS** ..... **xiii**

**ABSTRACT OF THE THESIS** ..... **xiv**

**1.0 INTRODUCTION** ..... **1**

**2.0 BACKGROUND AND LITERATURE REVIEW** ..... **3**

**2.1 DOMAINS OF REPRESENTATION FOR LINEAR DYNAMICS** ..... **3**

*2.1.1 The Physical Domain* ..... *3*

*2.1.2 Modal Analysis and the Modal Domain* ..... *4*

*2.1.3 The Fourier Transform and the Frequency Domain* ..... *6*

**2.2 TESTING AND TEST ANALYSES** ..... **8**

*2.2.1 Sampling Theory* ..... *9*

*2.2.2 Power Spectra and Power Spectral Density Estimations* ..... *10*

*2.2.3 Frequency Response Function Estimation* ..... *12*

*2.2.4 Modal Parameter Estimation* ..... *14*

**2.3 STATIONARY RANDOM PROCESSES** ..... **15**

*2.3.1 Wide-sense Stationary* ..... *15*

*2.3.2 Generating Realizations of Stationary Random Processes* ..... *16*

**2.4 OPTIMIZATION** ..... **18**

*2.4.1 Objective Functions* ..... *18*

*2.4.2 Algorithms for Optimization* ..... *19*

**2.5 ELECTRODYNAMIC SHAKER PHYSICS** ..... **20**

**2.6 ELECTRODYNAMIC SHAKER MODELING** ..... **22**

*2.6.1 Electro-Mechanical Models* ..... *23*

*2.6.2 Equivalent Electrical Models* ..... *28*

**2.7 EXPERIMENTAL DYNAMIC SUBSTRUCTURING BACKGROUND** ..... **30**

*2.7.1 Substructuring Domains* ..... *31*

*2.7.2 Frequency Based Substructuring* ..... *31*

*2.7.3 Dynamic Equilibrium and Interface Conditions in the Frequency Domain* ..... *32*

*2.7.4 Primal Assembly* ..... *35*

*2.7.5 Dual Assembly* ..... *35*

*2.7.6 Lagrange Multiplier Frequency Based Substructuring* ..... *36*

*2.7.7 Challenges to Frequency Based Substructuring ..... 37*

**3.0 EXPERIMENTATION AND ANALYSES ..... 40**

**3.1 ELECTRODYNAMIC SHAKER MODEL DEVELOPMENT ..... 40**

*3.1.1 Model Parameters ..... 41*

*3.1.2 Equations of Motion ..... 41*

*3.1.4 Shaker Model Validation Test setup ..... 45*

*3.1.5 Test Results ..... 47*

*3.1.6 Model Updating ..... 49*

**3.2 EXPERIMENTAL DYNAMIC SUBSTRUCTURING IMPLEMENTATION ..... 55**

*3.2.1 Substructure Modal Testing ..... 55*

*3.2.2 Substructuring Analysis ..... 58*

*3.2.3 DUT-Shaker Coupling Validation Test ..... 59*

*3.2.4 Substructuring Analysis Results ..... 63*

**3.3 SHAKER CAPABILITY ESTIMATION ..... 66**

*3.3.1 Transforming the Test Specification ..... 67*

*3.3.2 Transforming the Time Domain Signal ..... 72*

**4.0 DISCUSSION AND CONCLUSIONS ..... 79**

**4.1 DISCUSSION ..... 79**

*4.1.1 Shaker Modeling ..... 79*

*4.1.2 Experimental Dynamic Substructuring Implementation ..... 80*

*4.1.3 Shaker Capability Estimation ..... 83*

**4.2 CONCLUSIONS AND RECOMMENDATIONS ..... 84**

**5.0 REFERENCES ..... 86**

# LIST OF ABBREVIATIONS

ADC: Analog to digital converter

BARC: Box and Removable Component

DAQ: Data acquisition system/unit

DFT: Discrete Fourier transform

DOF(s): Degree(s) of freedom

DUT: Device under test

EMPC: Equivalent multipoint connection

FBS: Frequency based substructuring

FRF: Frequency response function

IDFT: Inverse discrete Fourier transform

LM-FBS: LaGrange multiplier frequency based substructuring

PDF: Probability density function

PSD: Power spectral density

RMS: Root mean square

TS: Transmission simulator

# LIST OF SYMBOLS

**M**/m: Mass matrix/mass value

**C**/c: Damping matrix/damping value

**K**/k: Stiffness matrix/stiffness value

**u**: Vector of response degrees-of-freedom

**f**: Vector of external input forces

**V/v**: Matrix of eigenvectors/eigenvector

**Λ**/λ: Matrix of eigenvalues/eigenvalue

**Φ**: Modal matrix

**Ω** /$\omega_n$: Diagonal matrix of natural frequencies/Natural frequency ($n^{th}$)

$\hat{\mathbf{M}}$: Modal mass matrix

$\hat{\mathbf{K}}$: Modal stiffness matrix

**ε**/$\zeta_n$: Diagonal matrix of damping ratios/Damping ratio ($n^{th}$)

η: Modal coordinate

j: Imaginary unit

ω: Frequency domain independent variable, in radians/second

t: Time domain independent variable, in seconds

N: blocklength in samples

**H**: Frequency response function matrix

$f_{max}$: Maximum resolvable frequency

$F_s$: Sampling frequency

Δt: Time resolution

Δ*f*: Frequency resolution

T: Sampling period, time

$S_x$: Linear spectrum

$G_{xx}$: Autopower spectrum

$G_{xy}$: Cross power spectrum

R: Resistance

L: Inductance

**Z**: Mechanical impedance

**g:** Vector of internal forces

**Γ**: Interface boundary

**L**: Boolean localization matrix

**B**: Signed Boolean mapping matrix

***l***: Vector of LaGrange multipliers

V: Voltage/EMF

q: Charge

K: Coupling coefficient

**M̃**: Modified electromechanical mass matrix

**C̃**: Modified electromechanical damping matrix

**K̃**: Modified electromechanical stiffness matrix

$e_{FRF/model}$: Error

**R**: Power spectral density

# LIST OF FIGURES

Figure 2.1.1 Domains of representation and how they are related. ..... 3

Figure 2.1.2 Discretization of a beam into a 3-DOF system of masses, springs, and dampers. ..... 4

Figure 2.2.1 Visualization of Welch's method for estimating power spectral density. ..... 12

Figure 2.2.2 Visual representation of the noise model for dynamic system measurements. ..... 13

Figure 2.3.1 A visual representation of the difference between stationary and ergodic. ..... 16

Figure 2.3.2 Visualization of stationary random signal generation process. ..... 18

Figure 2.5.1 Diagram of an electrodynamic shaker. ..... 20

Figure 2.5.2 Illustrations of the shaker's vibration modes. ..... 22

Figure 2.6.1 2-DoF shaker model capturing the isolation and suspension modes of the [10]. ..... 24

Figure 2.6.2 3-DoF shaker model with the body, armature, and stinger as the mechanical degrees of freedom [11]. ..... 25

Figure 2.6.3 3-DoF shaker model with the body, armature table and voice coil as the mechanical degrees of freedom [14]. ..... 26

Figure 2.6.4 6-DoF shaker model that captures out of axis motion of the shaker using rotational degrees of freedom [15]. ..... 27

Figure 2.6.5 2-DoF model of the shaker armature, assuming the shaker body dynamics are negligible [16]. ..... 28

Figure 2.6.6 Equivalent electrical circuit shaker models for different frequency ranges of operation [17]. ..... 29

Figure 2.6.7 Two-port network model of a shaker [18]. ..... 30

Figure 2.7.1 Assembly of two substructures R and S, at boundary nodes, $u_b$. ..... 32

Figure 3.1.1 Shaker electromechanical model diagram. ..... 40

Figure 3.1.2 Effects of changing the table mass on the three FRFs of interest. ..... 44

Figure 3.1.3 Shaker model validation test setup. The body accelerometer is behind the slip table housing. ..... 46

Figure 3.1.4 Shaker measured impedance. ..... 48

Figure 3.1.5 Shaker measured acceleration over voltage FRF. ..... 48

Figure 3.1.6 Shaker measured acceleration over current FRF. ..... 49

Figure 3.1.7 Comparison of the modelled and measured impedance of the small shaker. ..... 50

Figure 3.1.8 Comparison of the modelled and measured table acceleration over amplifier voltage FRF of the small shaker. ..... 50

Figure 3.1.9 Comparison of the modelled and measured table acceleration over amplifier current FRF of the small shaker. ..... 51

Figure 3.1.10 Comparison of the updated model and measured impedance of the small shaker. 53

Figure 3.1.11 Comparison of the updated model and measured table acceleration over amplifier voltage FRF of the small shaker. ..... 54

Figure 3.1.12 Comparison of the updated model and measured table acceleration over amplifier current FRF of the small shaker. ..... 54

Figure 3.2.1 Modal impact test setup. ..... 56

Figure 3.2.2 FRF measured and synthesized from modal parameters at point 17 of the BARC base. ..... 57

Figure 3.2.3 FRF measured and synthesized from modal parameters at point 129 of the BARC base. ..... 58

Figure 3.2.4 Setup of the substructure coupling validation test. ..... 60

Figure 3.2.5 Comparison of the impedance with the shaker alone vs when coupled with the BARC base ..... 61

Figure 3.2.6 Comparison of the table acceleration over current FRF with the point 17 acceleration over current FRF. ..... 62

Figure 3.2.7 Comparison of the table acceleration over voltage FRF with the point 17 acceleration over current FRF. ..... 62

Figure 3.2.8 Impedance estimated from substructure coupling compared to measured impedance. ..... 63

Figure 3.2.9 Acceleration over voltage FRF at Point 17 estimated from substructure coupling compared to measured acceleration over voltage FRF at Point 17. ..... 64

Figure 3.2.10 Acceleration over current FRF at Point 17 estimated from substructure coupling compared to measured acceleration over current FRF at Point 17. ..... 64

Figure 3.2.11 Acceleration over voltage FRF at Point 129 estimated from substructure coupling compared to measured acceleration over voltage FRF at Point 129. ..... 65

Figure 3.2.12 Acceleration over current FRF at Point 129 estimated from substructure coupling compared to measured acceleration over current FRF at Point 129. ..... 65

Figure 3.3.1 Inverse FRFs to use for transforming test specification to electrical requirements. 68

Figure 3.3.2 Estimate of the voltage input spectrum required for a random vibration test compared to the measured voltage input of a test using the same specification. ..... 69

Figure 3.3.3 Estimate of the current input spectrum required for a random vibration test compared to the measured current input of a test using the same specification. ..... 70

Figure 3.3.4 Comparison of a synthesized time signal satisfying the test specification vs the measured acceleration achieved from that specification. ..... 73

Figure 3.3.5 Comparison of estimates for the input voltage signal to the measured input voltage signal. ..... 75

Figure 3.3.6 Comparison of estimates for the input current signal to the measured input current signal. ..... 76

Figure 3.3.7 Synthesized and measured (a) voltage and (b) current data histograms compared to their normal distribution fits. ..... 78

# LIST OF TABLES

Table 3.1.1 Model parameter sensitivities ..... 45

Table 3.1.2 Chosen model parameters ..... 53

Table 3.3.1 RMS and Peak Value Estimates Comparison for Test Specification Transformation ..... 71

Table 3.3.2 RMS and Peak Value Estimates Comparison for Time Domain Signal Transformation ..... 74

# ACKNOWLEDGEMENTS

I would like to acknowledge and thank my committee, Professor Qiang Zhu, Professor Chuck Farrar, and especially my chair and advisor Professor Michael Todd. In addition, I would like to acknowledge and thank my mentors at Los Alamos National Laboratory, Dr. John Schultze and Dr. Dustin Harvey for their guidance on this project. Finally, I would like to acknowledge my first mentors at LANL, Dr. Adam Wachtor and Dr. Eric Flynn for introducing me to academic research and their continued support in my career and education goals.

The work presented in this thesis was funded by the Delivery Environments program under the Office of Engineering and Technology Maturation at Los Alamos National Laboratory. I would like to thank the program manager Dr. Antranik Siranosian and my group leader Andrew Morello for allowing me to pursue this project as part of this degree.

This thesis, in portion, is a reprint of material as it appears in the Conference Proceedings of the 41st International Modal Analysis conference, 2023. Peter H. Fickenwirth, Michael D. Todd, John F. Schultze, Dustin Y. Harvey, Springer, 2023. The thesis author was the primary investigator and author of this paper.

# ABSTRACT OF THE THESIS

Electrodynamic Shaker Capability Estimation Through Experimental Dynamic Substructuring

by

Peter Hans Fickenwirth

Master of Science in Structural Engineering with a Specialization in Structural Health Monitoring and Non-Destructive Evaluation

University of California San Diego, 2023

Professor Michael Todd, Chair

Electrodynamic shaker systems are an essential tool in shock and vibration testing of dynamic environments. However, the specific performance capability of these systems is difficult to characterize. The dynamics of the shaker itself, the device under test and the specific test configuration used all couple to create a dynamic response unique to each test. Poorly predicted limitations in shaker capability affect the ability to achieve test specifications, delay testing schedules, and create difficulties for choosing test equipment. To predict shaker capability for a specific test configuration prior to setup, a lumped parameter model of the shaker system and a modal model of a device under test was developed. These models were then analytically coupled using LaGrange multiplier frequency based substructuring to estimate their coupled frequency response functions. The coupled frequency response functions were used to predict electrical inputs required to meet a given test specification. These input requirements were finally compared

to a validation test using the specification and setup. Input requirements estimated using the substructuring estimated frequency response functions showed significant error. However, results using an ideal frequency response function showed very little error. These results indicate that with a better method of experimental dynamic substructuring employed it would be possible to accurately predict shaker capability for a given test configuration prior to setup.

# 1.0 INTRODUCTION

Historically, equipment for vibration testing of assemblies has been selected based on past tests, engineering judgement, and simple calculations using Newton's second law of physics. Electrodynamic shaker manufacturers provide data sheets with general limits to shaker capability regarding peak force, maximum velocity, and maximum stroke outputs. Performance curves in the frequency spectrum that show how these different output limits affect performance may also accompany shakers. However, these systems have complicated dynamics, and the standards for testing them do not capture the full dynamic range they may be operated in. Further, these limits only account for the capabilities of the shaker, and not the amplifier being used to run it. The dynamics of the shaker may cause antiresonances that absorb the energy input to the system, resulting in bands where the amplifier is overloaded before the maximum force output of the shaker is achieved. Conversely, resonances in the shaker system may cause difficulty in control as small electrical inputs result in large mechanical responses. Further, the device under test, its various orientations being tested, the fixturing required for testing, and even the software used to control the system all influence the dynamics of the shaker system.

A more detailed understanding of these systems can be achieved through modeling of the shaker. Updating the model with experimentally collected data further ensures an accurate characterization of its performance. Lumped parameter models have been shown to capture the dynamics of electrodynamic shakers and predict the outcomes of random vibration tests. These models are effective at predicting test outcomes for simple test articles, but further information is needed still. More complex test articles and setups on the shaker may strongly influence the dynamics of the now coupled system. These coupled dynamics are easily determined once the test has been setup on the shaker, but limitations before this point are difficult to predict, often resulting

in testing delays and lost time on the shaker. Further, understanding the coupled dynamics of article with multiple shakers allows better selection of the testing equipment available.

Experimental dynamic substructuring is a class of methods for estimating the dynamics of an assembly based on the dynamics of the individual components. LaGrange multiplier, frequency-based substructuring is a particular technique that utilizes the frequency response functions of the individual components to estimate their coupled dynamics. This coupling is achieved through equations developed based on the interface boundary conditions between the components. These conditions are defined by a signed Boolean matrix which localizes the interfaces and uses LaGrange multipliers to represent the magnitudes of the internal forces at these interfaces.

Frequency response functions are estimated from the updated shaker model, and modal impact testing offers a convenient means of experimentally measuring the frequency response functions on a test article. LaGrange-multiplier frequency based substructuring is then used to couple these two sets of FRFs together and analytically determine the coupled dynamics of the two prior to physical test setup. The estimate of these dynamics is then used to assess the required electrical inputs from the amplifier to achieve a test specification given in the form of a power spectral density. This coupling may even be performed with multiple shaker models to determine the best equipment for the test. The goal of this work is to estimate the frequency response functions relating the acceleration responses of potential control locations to the electrical inputs of an electrodynamic shaker in order to predict the feasibility of a test, without the need for physically setting up the test.

# 2.0 BACKGROUND AND LITERATURE REVIEW

## 2.1 Domains of Representation for Linear Dynamics

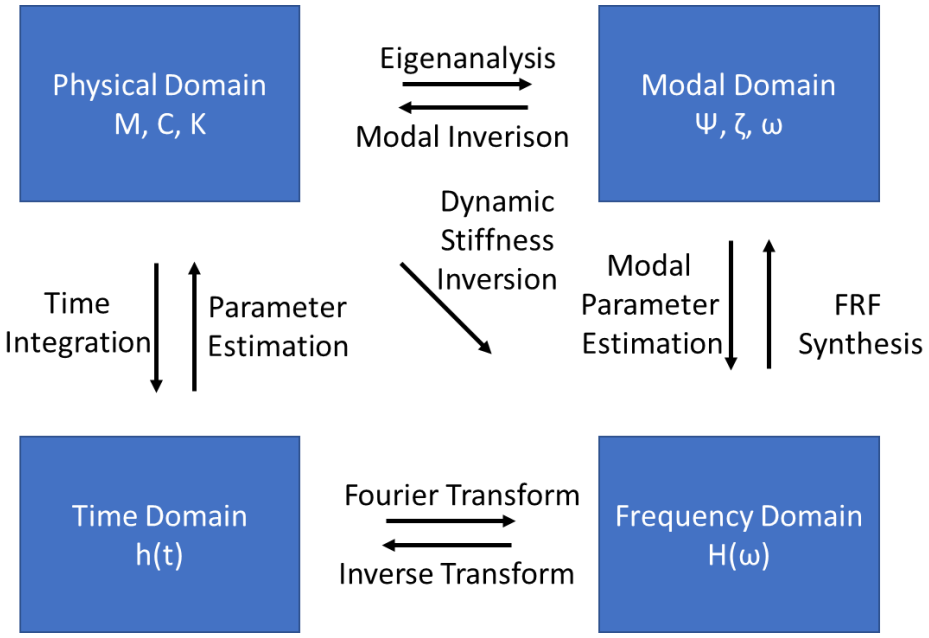


Figure 2.1.1 Domains of representation and how they are related.

When modeling linear dynamic systems there are many domains of representation that can be used. These include the physical, modal, time, Laplace, frequency, and state space domains, among others. Three main domains of representation are used in this work: the physical domain, the modal domain, and the frequency domain. The final section utilizes the time domain as well. Ref. [1] discusses the different domains of representation for dynamic systems, and specifically their uses in dynamic substructuring, more thoroughly. Figure 2.1.1 shows how the different domains of representation utilized in this work are related to one other.

### *2.1.1 The Physical Domain*

In the physical domain, linear dynamic systems may be represented by mass, stiffness, and damping matrices. These properties are continuously distributed throughout a body but are often

discretized for analytical models. In this work these properties are discretized into lumped mass elements which are connected by springs and dampers to represent an electrodynamic shaker.

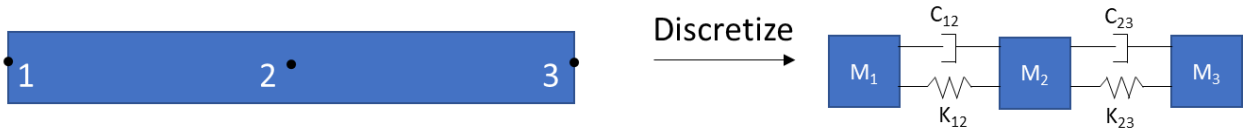


Figure 2.1.2 Discretization of a beam into a 3-DOF system of masses, springs, and dampers.

Consider a beam as an example, shown in figure 2.1.2. The beam is discretized into 3 lumped masses connected by springs and dampers. The mass, damping and stiffness matrices in the physical domain are then

$$\mathbf{M} = \begin{bmatrix} m_1 & 0 & 0 \\ 0 & m_2 & 0 \\ 0 & 0 & m_3 \end{bmatrix}, \mathbf{C} = \begin{bmatrix} c_{12} & -c_{12} & 0 \\ -c_{12} & c_{12}+c_{23} & -c_{23} \\ 0 & -c_{23} & c_{23} \end{bmatrix}, \mathbf{K} = \begin{bmatrix} k_{12} & -k_{12} & 0 \\ -k_{12} & k_{12}+k_{23} & -k_{23} \\ 0 & -k_{23} & k_{23} \end{bmatrix}.$$

The matrices are then assembled via Newton's 2nd law into the equations of motion for the system,

$$\mathbf{M\ddot{u}} + \mathbf{C\dot{u}} + \mathbf{Ku} = \mathbf{f}, \tag{2.1}$$

where **u** is the vector of responses at the degrees of freedom (DOFs), and **f** is the vector of input forces to the system. These equations can be used to calculate the response of the system given an input, but the coupling between the different equations makes it difficult. Instead, modal analysis is often used.

*2.1.2 Modal Analysis and the Modal Domain*

Modal analysis is a method of decoupling the relationships between the different masses, stiffness values, and damping values in the physical representation of a system. The matrices are decoupled by diagonalization using the eigenvalue decomposition. Ref. [2] provides more depth

on the eigenvalue decomposition and other linear algebra fundamentals. The eigenvalue decomposition solves the characteristic equation,

$$\mathbf{Av} = \boldsymbol{\lambda}\mathbf{v}. \tag{2.2}$$

Solving Equation 2.2 gives a diagonal matrix of eigenvalues $\boldsymbol{\Lambda}$ and a matrix $\mathbf{V}$ of column eigenvectors $\mathbf{v}$, each of which have the property described in Eq. 2.2. These eigenvectors and eigenvalues can then be used to make a diagonal representation of $\mathbf{A}$. The eigenvectors are used to diagonalize the matrix $\mathbf{A}$ by projecting it into a new space,

$$\boldsymbol{\Lambda} = \mathbf{V}^{-1}\mathbf{AV}. \tag{2.3}$$

When applied to the mass and stiffness matrices of a dynamic system, the stiffness matrix is decomposed with respect to the mass matrix to establish the analogous eigenvalue problem

$$\mathbf{Kv} = \mathbf{M}\boldsymbol{\lambda}\mathbf{v}. \tag{2.4}$$

The equation is often rewritten as

$$(\mathbf{K} - \mathbf{M}\boldsymbol{\lambda})\mathbf{v} = \mathbf{0}. \tag{2.5}$$

The solution of the decomposition yields the diagonal matrix of eigenvalues, which are interpretable as the squares of the system's natural frequencies, and the matrix of column eigenvectors, which are interpretable as the mode shapes associated with those natural frequencies. The matrix of eigenvectors is referred to as the modal matrix. Typical dynamic systems are reciprocal, yielding symmetric mass and stiffness matrices, so the modal matrix is an orthogonal matrix and has the property that its transpose is its inverse,

$$\boldsymbol{\Lambda} = \begin{bmatrix} \omega_1^2 & \cdots & 0 \\ \vdots & \ddots & \vdots \\ 0 & \cdots & \omega_n^2 \end{bmatrix}, \boldsymbol{\Phi} = [\mathbf{v}_1, \quad \ldots, \quad \mathbf{v}_n].$$

The modal matrix is then used to transform the equations of motion in Equation 2.1 into the modal domain. In the modal domain the set of equations is generally uncoupled as the $\mathbf{M}$ and

**K** matrices have been diagonalized and are instead represented by the modal mass matrix $\hat{\mathbf{M}}$ and the modal stiffness matrix, $\hat{\mathbf{K}}$. In some cases repeated roots exist, coupling together equations, forming a block diagonalization instead. Typically, the mode shape vectors are normalized by the square roots of the modal masses, so the modal mass matrix is simply the identity, **I**. When this is done, the modal stiffness matrix is then equivalent to the eigenvalue matrix. Note that the damping matrix **C** was not diagonalized in the modal decomposition. Instead damping ratios, ζ, are estimated to approximate the damping matrix. Often this is done by a proportional damping model, where the **C** matrix is approximated as a linear combination of the **K** and **M** matrices, allowing it to be diagonalized. The equations of motion may now be written as a set of decoupled equations,

$$\ddot{\eta} + 2\zeta_n\omega_n\dot{\eta} + \omega_n^2\eta = \hat{f}_n, \tag{2.6}$$

where the number of equations n is equal to the number of modes. The modal coordinate η, and the modal force, $\hat{f}$, can be determined by transforming the force and response vectors **f** and **u** [3],

$$\mathbf{u} = \boldsymbol{\Phi}\boldsymbol{\eta} \text{ and } \mathbf{f} = \boldsymbol{\Phi}\hat{\mathbf{f}}. \tag{2.7}$$

Using these equations, the response of the system to a force may be calculated to get the time-domain response.

*2.1.3 The Fourier Transform and the Frequency Domain*

The modal and physical domains are time-domain representations of systems, as the equations are time-dependent. Just as the modal domain decomposes the spatial representation into independent components, the frequency domain decomposes time signals into independent frequency components, or sinusoidal components, using the Fourier transform. Given a continuous time-domain signal x(t), the continuous Fourier transform X(ω) is

$$\mathrm{X}(\omega) = \int_{-\infty}^{\infty} x(t)e^{-j\omega t}\,dt, \tag{2.8}$$

where ω is frequency in radians per second. The Fourier transform is a widely used method of analyzing time signals to understand their spectral content. In addition, certain operations, such as convolution, are more conveniently performed in the frequency domain. Filtering of time-domain signals is often performed in the frequency domain because of this convenience. When measured, time domain signals are discretized for digital representation on computers. When analyzing a discretized time signal x[n] of length N, the discrete Fourier transform is used,

$$\mathrm{X}_k = \frac{1}{N}\sum_{n=0}^{N-1} x[n]e^{-j\left(\frac{2\pi}{N}\right)kn}, \tag{2.9}$$

where $X_k$ is the sequence of Fourier coefficients representing the signal in the frequency domain. The frequencies at which the Fourier coefficients are calculated depends on the length of the signal and the time resolution at which the signal is sampled [4]. These concepts will be discussed further in the next section.

In the frequency domain dynamic systems are modeled by their FRFs. These functions describe how a dynamic system will respond to an excitation on a frequency basis. FRFs can be calculated from either set of equations of motion in the previous subsections, Equations 2.1 and 2.6. When using the matrix representations from the physical domain, the direct frequency response method can be employed,

$$\mathbf{H}(\omega) = (-\omega^2\mathbf{M} + \mathrm{j}\omega\mathbf{C} + \mathbf{K})^{-1}, \tag{2.10}$$

where **H(**ω) is the frequency response function matrix of the system. **H(**ω) is calculated on a frequency line basis, with ω being the frequency, in radians per second, at that line. Alternatively, the FRFs of a system may be determined based on the modal parameters described previously,

$$\mathbf{H}(\omega) = \boldsymbol{\Phi}(\boldsymbol{\Omega}^2 + 2\mathrm{i}\omega\boldsymbol{\Omega}\boldsymbol{\varepsilon} - \omega^2\mathbf{I})^{-1}\boldsymbol{\Phi}^{\mathrm{T}}, \tag{2.11}$$

where **H(**ω) is again the frequency response function matrix, **Ω** is a diagonal matrix of the natural frequencies, $\omega_n$, **ε** is a diagonal matrix of the damping ratios, $\zeta_n$, and **I** is the identity matrix. As with equation 2.10, **H(**ω) is calculated on a frequency line basis, with ω being the frequency, in radians per second, at each line [1]. These FRF calculations will later be used to determine FRFs from the lumped-parameter shaker model and the DUT modal model. FRFs may also be calculated from experimental data, which will be discussed in the next section.

### 2.2 Testing and Test Analyses

Modal testing and analysis are essential tools for shock and vibration testing. Modal testing and analysis are used to characterize the DUT, while random vibration testing is used to characterize the shaker's dynamics. Many concepts and analyses apply to both techniques. Ref. [3] provides comprehensive guide for modal testing and analysis, while [5] is an extensive guide to vibration testing concepts. Modal impact testing is used to characterize a dynamic system by inputting a force on the system with an impact hammer. The impact hammer contains a load cell to measure the force imparted, and accelerometers measure the response acceleration. For modal shaker testing, a stinger attached to a load cell is used to avoid cross-axis input and to measure the force imparted. In vibration and mechanical shock shaker testing, an electrodynamic shaker is used to impart a force on a test article, and accelerometers are again used to measure the response. The force is typically not measured, but instead the test is controlled to a response acceleration in order to approximate a previously characterized service environment. In both types of testing sampling requirements, power spectrum calculations, and frequency response function calculations play a large role in the acquisition and analysis of data.

*2.2.1 Sampling Theory*

In testing, data is collected using a data acquisition unit (DAQ) with an analog to digital converter (ADC). An ADC converts continuous analog signals into discretized digital signals for storage, analysis, and reporting on computers. The parameters of this conversion are paramount to collecting usable data from a test. The first test parameter to be determined is the sampling rate. This is the rate at which the analog signal is discretized in time. The Nyquist-Shannon sampling theorem dictates that the highest resolvable frequency of a sampled signal is at half the sample rate, referred to as the Nyquist frequency,

$$f_{max} < \frac{F_s}{2}. \tag{2.12}$$

Frequencies in the signal above the Nyquist frequency are unable to be resolved and will erroneously appear as lower frequencies in a phenomenon called aliasing. Therefore, the sampling frequency should be high enough to capture the highest frequency of interest, and the signal should be low pass filtered at or below the Nyquist frequency to prevent aliasing errors. The sampling frequency is the inverse of the time resolution,

$$\Delta t = \frac{1}{F_s}. \tag{2.13}$$

The next parameter to consider is the desired frequency resolution of the analyzed signal in the frequency domain. The frequency resolution is the inverse of the time-length of the acquisition,

$$\Delta f = \frac{1}{T}. \tag{2.14}$$

Time-domain acquisition must be long enough to reach the desired frequency resolution, but not so long that the dataset is unmanageable by the processing software. This leads to the final

sampling parameter, block length, or the number of samples acquired. Block length increases with finer time and frequency resolutions,

$$N = \frac{T}{\Delta t}. \tag{2.15}$$

Choosing two of these sampling parameters determines the remaining parameters, so engineering choices must be made to balance resolutions, dataset sizes, and time lengths of acquisition [3][4].

### *2.2.2 Power Spectra and Power Spectral Density Estimations*

The autopower spectrum estimation is one of the most common analyses performed in vibration testing. Power spectra are calculated to understand the distribution of a signal's energy in the frequency domain. For broadband random signals the power spectrum is often normalized by the frequency resolution used. This normalization is needed to compare signals to one another, as the power spectrum amplitude will increase with decrease in frequency resolution, just as the amplitude of a histogram increases when fewer bins are used. Normalizing by frequency resolution results in a power spectral density (PSD) estimate that removes this effect and allows different signals to be more easily compared. In modal testing, PSDs are used to understand the energy input to the system as well as the measured response, and power spectra are used to calculate frequency response functions [3]. In vibration testing, PSDs are used to specify tests as well as to understand the response of the test article [5].

The autopower spectrum is the Fourier transform of the autocorrelation function of a signal. It may be calculated either by convolving the signal with itself in the time domain, or equivalently taking the discrete Fourier transform (DFT) of the signal and multiplying by its complex conjugate,

$$G_{xx} = S_x S_x^*, \qquad (2.16)$$

where $G_{xx}$ is the autopower spectrum, $S_x$ is the DFT of the signal, or linear spectrum, and $S_x^*$ is the complex conjugate of the linear spectrum. Note the autopower spectrum will be positive and real-valued. Alternatively, multiplying by the conjugate of a different signal gives the cross-power spectrum,

$$G_{xy} = S_x S_y^*. \qquad (2.17)$$

From here the PSD may be calculated by normalizing by the frequency resolution, the inverse of the total period measured.

These calculations are accurate when a signal is either entirely captured by the sampling window or is perfectly periodic within it. In modal testing, impact excitation and burst random excitation are two methods used to meet this condition. However, these conditions are not always met, especially in vibration testing, where tests may last anywhere between minutes and days. When these conditions are not met, errors are introduced into the spectral estimate called "leakage," where energy is spread across multiple bins, reducing the true magnitude in a particular bin and transferring that information into the surrounding frequency bins. To reduce leakage, lag weighting window functions are often applied to signals to force them to meet the requirements of the DFT. An overview of common window functions and their effects on spectral estimates can be found in Ref. [3].

The most common method for estimating the PSD of a random signal is Welch's method because it is asymptotically unbiased [4]. The signal is broken up into smaller samples and windowed. Usually, segments are chosen with a 50% overlap to maximize the number of segments and reduce the loss of information from windowing. Then the DFT of each segment is calculated and multiplied by its conjugate to estimate the power spectrum for that segment. These estimates

are called periodograms. The set of periodograms is then averaged together to estimate the autopower spectrum. The PSD is finally found by normalizing by the frequency resolution [4]. Figure 2.2.1 gives a visual representation of the method.

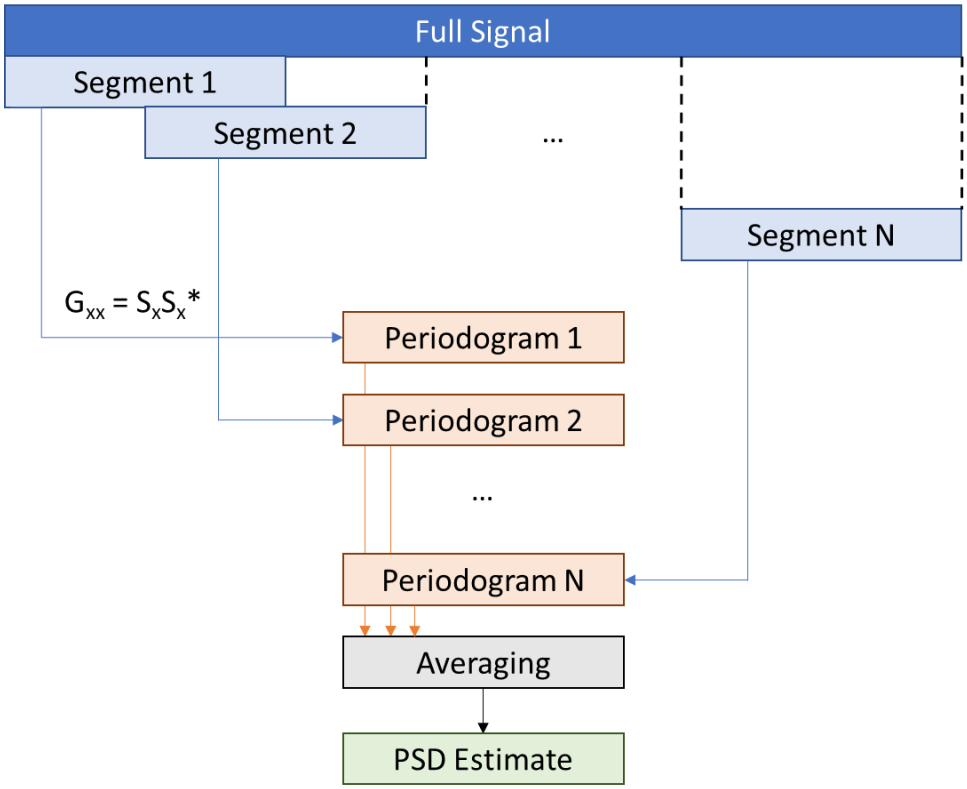


Figure 2.2.1 Visualization of Welch's method for estimating power spectral density.

*2.2.3 Frequency Response Function Estimation*

Frequency response functions are functions that describe the behaviors of dynamic systems in the frequency domain. FRFs relate the input force to a system at a given location to the response at another location. FRFs are organized into three-dimensional matrices, with dimensions of reference, or input, locations, response locations, and frequency line. In modal testing FRFs are used to characterize systems and for modal parameter estimation. In shock and vibration testing,

FRFs are used to estimate required excitation inputs for test specifications, assess control locations, and to transform test specifications to change control locations that might be difficult to control successfully.

Ideally, no noise exists on measurements, and the FRF is just the ratio of the measured input and output linear spectra from a system,

$$S_y = HS_x. \tag{2.18}$$

However, noise exists on all measurements made and must be accounted for. A noise model of measurements is shown in figure 2.2.2.

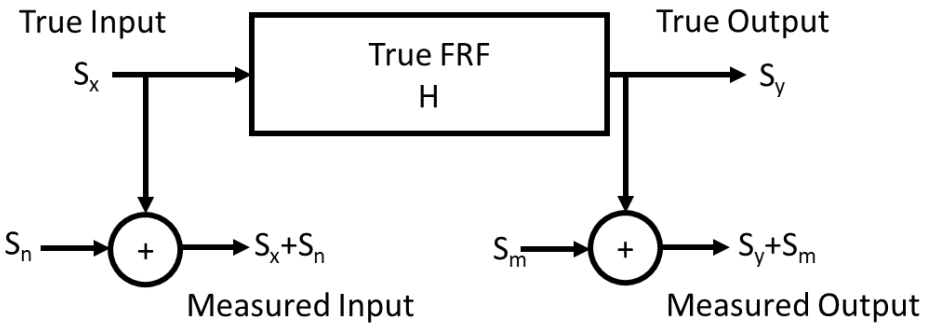


Figure 2.2.2 Visual representation of the noise model for dynamic system measurements.

In testing there are two common methods of FRF estimation, $H_1$ and $H_2$, used to minimize the effects of measurement noise. The $H_1$ estimator assumes no noise is present on the input ($S_n$ = 0) and minimizes noise on the output,

$$H_1 = \frac{G_{yx} + G_{mx}}{G_{xx}} \rightarrow H_1 = \frac{G_{yx}}{G_{xx}}. \tag{2.19}$$

If the noise on the output measurement is uncorrelated to the input, $G_{mx}$ will go to zero as the number of averages of the spectrum goes to infinity. While this formulation minimizes the effect of output noise, the assumption that no noise exists on the input results in a bias toward

underestimating the true FRF. When using transient inputs, a force-exponential window is often applied to the input signal to minimize the noise on the channel after the excitation has completed.

The $H_2$ estimator assumes no noise is present on the output ($S_m = 0$) and minimizes noise on the input,

$$H_2 = \frac{G_{yy}}{G_{xy} + G_{ny}} \rightarrow H_2 = \frac{G_{yy}}{G_{xy}}. \tag{2.20}$$

Similarly, if the noise on the input is uncorrelated to the output, $G_{ny}$ will go to zero as the number of averages of the spectrum goes to infinity. This formulation minimizes the effect of input noise, but again, the assumption that no noise exists on the output results in a bias toward overestimating the FRF [3].

There are three forms of FRF, depending on the response type measured. The FRF relating displacement to force input is referred to as receptance, velocity response as mobility, and acceleration response as accelerance. Accelerance is the most common type of FRF measured experimentally, while receptance is easily calculated from models. Differentiating FRFs in the frequency domain is performed by multiplying by jω on a frequency line, ω, basis, while integrating is performed by dividing by jω [5].

### *2.2.4 Modal Parameter Estimation*

Modal parameter estimation refers to a class of techniques used to identify the mode shapes, natural frequencies, and damping of a dynamic system based on measured FRFs. Modal parameter estimation can be achieved with many algorithms, but the PolyMAX algorithms developed by LMS and implemented in Siemens LMS Testlab, and others like it, have become the standard for estimation [3]. This work utilized the ATA Engineering package IMAT's orthogonal polyreference, or OPoly, algorithm for modal parameter estimation. These algorithms are often

proprietary and utilize various procedures and processes for estimating the poles, which contain information about the natural frequencies and damping ratios of the system, and the residues, which contain information about the mode shapes. Modal parameter estimation is often performed only in a frequency band of interest, with the effects of modes outside the band of interest estimated as upper and lower residual terms.

## 2.3 Stationary Random Processes

Many of the analyses and processes in modal testing and random vibration testing come from probability and statistics, particularly from the theories of random variables and processes. Random vibrations are usually represented as stationary random processes. Mechanical shocks are also represented as random processes but are nonstationary.

### *2.3.1 Wide-sense Stationary*

A random process is considered wide-sense stationary if its mean and variance are independent of sample, or in the case of random vibrations, time, and its autocorrelation is only dependent on difference in sample (time), also called lag. In this definition, the independence of time does *not* mean any time during a single realization of the process. Instead, it means that the mean and variance of N numbers of realizations of the process should be the same regardless of the time the realizations are sampled at. If the mean and variance are represented by any time-window sample of a single realization of the process, it is called ergodic. Figure 2.3.1 visually represents this difference. When stationary and ergodic signals are transformed by linear, time invariant systems, the resulting signals retain these properties [4].

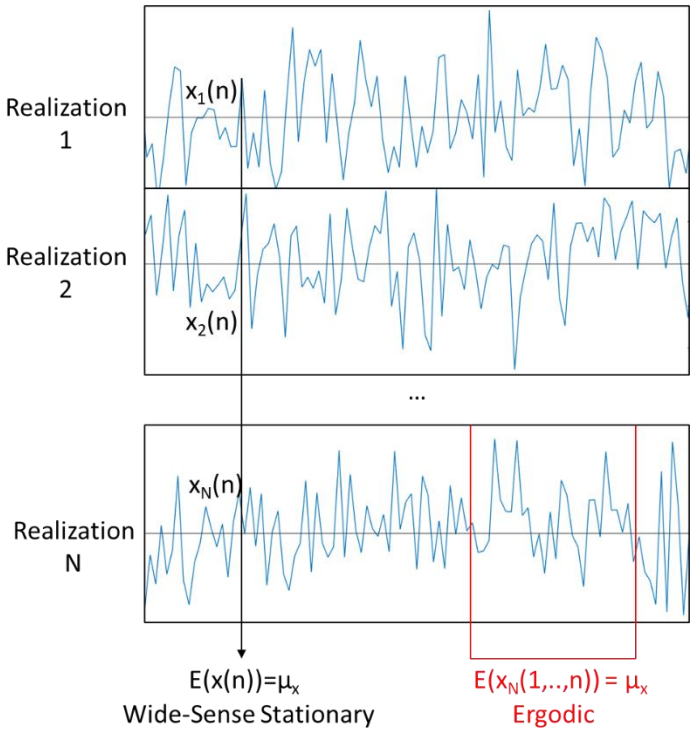


Figure 2.3.1 A visual representation of the difference between stationary and ergodic.

*2.3.2 Generating Realizations of Stationary Random Processes*

Commercial control software generates stationary random vibrations which satisfy given test profiles. This work creates realizations of such signals for performing capability estimation of shakers using representative signals. The method used in this work is derived from [6], originally described for FORTRAN, but adapted to MATLAB. The algorithm generates the desired amplitude spectrum for the signal, associates randomized phase, and then uses the inverse discrete Fourier transform to create a real signal in the time domain.

First, the power spectral density is defined at all frequency lines. The PSD must be 0 at the zero-frequency line and Nyquist line to generate a zero-mean realization. The number of spectral lines will be N/2+1 for a desired length N time signal. Generally, the PSD is defined at a limited number of break points, so the desired PSD between those points must be interpolated.

Now a linear spectrum with this PSD must be generated. First, the PSD is “unnormalized” to find the power spectrum by multiplying by the frequency resolution. The frequency resolution is defined by the desired length of the time signal and the required sample rate, at least 2 times the maximum frequency. The PSD is usually defined as a single-sided spectrum, and if so, the power spectrum must be divided by 2 at all points except the zero-frequency line and Nyquist line, as a two-sided linear spectrum is being formed. For a zero mean signal these should be zero anyway. Next, because the magnitude of the power spectrum is the square of the amplitude of the linear spectrum, the square root of the magnitudes is taken. These amplitudes are then assigned a randomized phase component. In this work this was achieved using the *randn* function in MATLAB, a pseudorandom, gaussian distributed noise generator. This completes generating the linear spectrum for the positive frequencies. For the signal to be real when inverse discrete Fourier transformed into the time domain, the signal must be Hermitian. A Hermitian signal is even on the real line, and odd on the imaginary line, so this is done by assigning the negative frequencies as the complex conjugates of the real frequencies just developed.

Finally, the inverse discrete Fourier transform is taken to calculate the signal in the time domain. Figure 2.3.2 shows a visualization of the process.

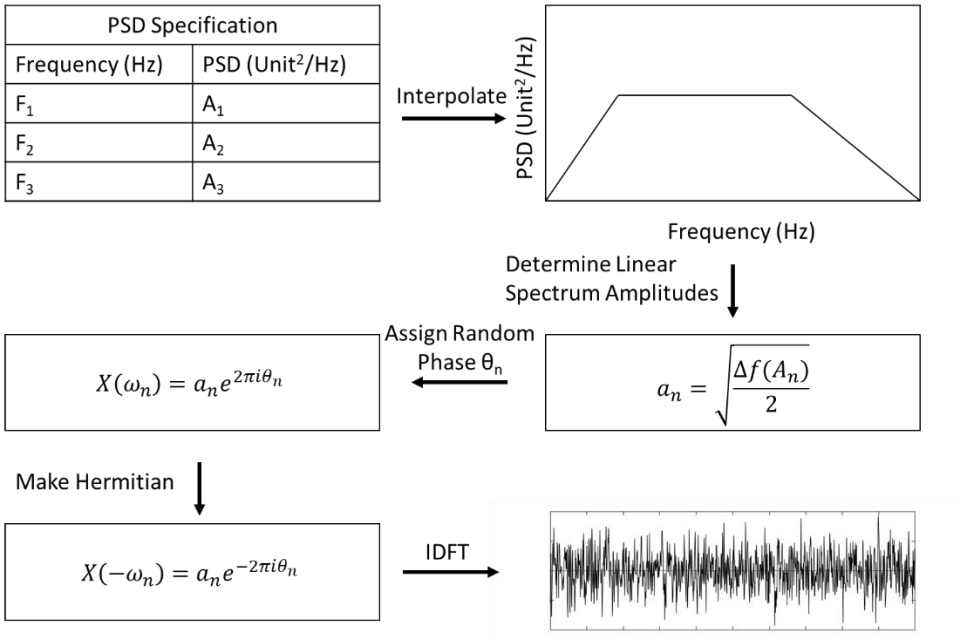


Figure 2.3.2 Visualization of stationary random signal generation process.

## 2.4 Optimization

Optimization is a rich and complex field with a long history and constantly evolving future. There are many periodic journals dedicated to the topic with new research published each year. This work just lightly touches on the topic.

### *2.4.1 Objective Functions*

Optimization methods seek to maximize or minimize some objective function subject to given constraints. The objective function is often an error quantification, and the goal is to minimize that function. The choice and design of the objective function is dictated by the problem being solved. Multiple objective functions may successfully achieve the same desired solution, so the design of the function requires engineering judgement and decisions. Certain algorithms for optimization have requirements for the formulation of the objective function, such as

differentiability. Often, tradeoffs are made between desired outcomes which must be captured and balanced in the objective function. This balance may be achieved by creating a multiobjective function, the summation of two functions weighted by their importance to the solution. Finally, constraints are applied to the problem which bound the solution to some reasonable set of outcomes. Constraints are necessary because sometimes the global minimum of the objective function may result in a solution that is not physically realizable. In this work, optimization is used to update a shaker model, so the optimal solution is constrained to having positive parameters, as negative mass, stiffness, or damping is not representative of the usual physical properties of dynamic systems [7].

### *2.4.2 Algorithms for Optimization*

There are many algorithms for optimization with new methods proposed all the time. Traditional techniques use calculus, statistical methods, and stochastic processes to find minima within the solution space of the objective function. First order algorithms, such as the gradient descent, use the first derivative of the objective function to choose how to search within the space. Second order algorithms, such as the secant method, use the second derivative. More modern techniques use a variety of approaches to search for the global minimum in the solution space. These techniques have similar features, such as the use of stochastic and probabilistic methods, utilization of trial and error and other heuristic approaches, and often are modeled after the behaviors of grouping and swarming species. Examples of such techniques are particle swarm optimization and genetic algorithms [7].

## 2.5 Electrodynamic Shaker Physics

Electrodynamic shakers are among the most common machines used for shock and vibration testing. The operating principle of an electrodynamic shaker is like that of a loudspeaker, though heavier and more robust. A coil of wire is suspended in a fixed magnetic field, and a current is passed through the coil. The current in the coil creates an electromagnetic field. The interaction between the two fields causes an axial force on the coil, resulting in motion. When an alternating current is used, oscillating motions can be generated. The fixed magnetic field can be generated by a permanent magnet or an electromagnet.

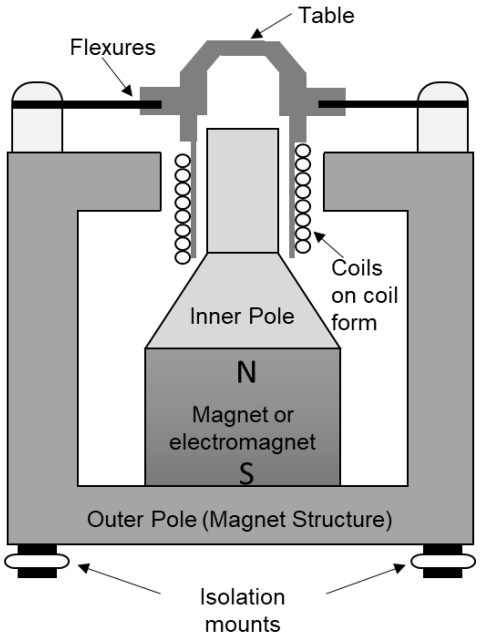


Figure 2.5.1 Diagram of an electrodynamic shaker.

A typical shaker design is shown in Figure 2.5.1. The armature is formed by the load table and the voice coil. The table is the location where a device under test is attached to the shaker. The voice coil forms the electromagnet. The force produced by the shaker is proportional to the current in the coil, and the velocity proportional to the voltage. The wires that form the coil are made of heavy conductors to allow high currents to flow through, achieving higher force outputs.

The armature is suspended in a radial magnetic field using a suspension system, or flexures, that allow axial motion, but prevent moments and cross-axis motion at the table. These flexures also keep the voice coil centered in the field. The radial magnetic field is achieved by using either an axial permanent magnet or DC electromagnet, referred to as field coils, connected to a magnetic circuit. The inner pole of the circuit will be connected to one pole of the axial magnet, while the outer pole the other. The circuit is made of permeable materials that creates, in the case of the diagram shown, a south-polarized magnetic disk. The inner pole is north-south polarized, thus achieving a radial field. The gap between the inner and outer poles are minimized to maximize the intensity of the magnetic field. The voice coil must be larger than the thickness of the outer pole to ensure the coils stay within the field throughout the entire stroke of the shaker.

The proximity of the coils to the magnetic pole pieces creates an inductive component to the electronic behavior of the shaker, resulting in a complex impedance. The resistance, R, of the coil represents the minimum impedance of the shaker, and the inductance, I, results in an increasing impedance with frequency. In addition to the inductive component, the motion of the coil within the field generates a voltage across it that is proportional to the velocity. This voltage is referred to as a back emf in the electrical domain. Therefore, the mechanical and electrical portions of the shaker are coupled to one another through both the electrical inputs to the system as well as its mechanical motion [8][9]. For small displacements this coupling can be described by a single coefficient multiplied by the relative velocity of the coil and shaker body for the back EMF and multiplied by the current to represent the force.

Finally, shakers are often isolated from the surrounding environment through the use of isolation mounts. These mounts prevent the transfer of energy from the shaker into the

environment which may cause excessive noise and vibration. However, it also adds a degree of freedom to the dynamics of the system.

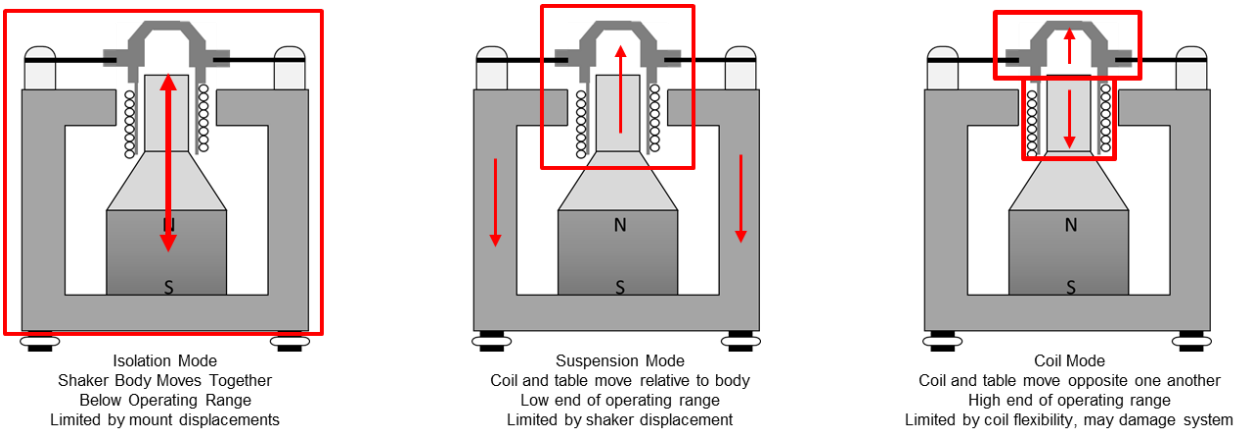


Figure 2.5.2 Illustrations of the shaker's vibration modes.

An isolated shaker system typically displays three main modes of vibration, illustrated in Figure 2.5.2. The first of these modes is referred to as the isolation mode. In this mode, the entire shaker moves almost as a rigid body on its isolation mounts, with very little relative motion between the different components. This mode typically occurs outside the effective frequency operating range of the shaker. The second mode of vibration usually occurs in the low range of the shaker's operating range and is called the suspension mode. In this mode the armature moves rigidly with relation to the body of the shaker. The final mode of vibration is the coil mode, in the high end of the shaker's operating range. In this mode the coil and table move out of phase with one another, has the potential to break the shaker, and often creates difficulty in controlling vibration at that frequency [9].

## 2.6 Electrodynamic Shaker Modeling

Almost all approaches to modeling electrodynamic shakers attempt to capture the dynamics of the three main modes of the shaker previously discussed. Many shaker models developed are

lumped parameter electro-mechanical models. These models are convenient because they discretize systems into simple elements that approximate the real system and can be solved with ordinary differential equations. These types of models are used for both modeling electrical circuits and mechanical systems, which lends itself to modeling these electro-mechanical machines. Other modeling approaches model the shakers as purely electrical systems.

### *2.6.1 Electro-Mechanical Models*

In their work on virtual shaker testing Martino and Harri [10] modeled an electrodynamic modal shaker by treating the body and the armature as vertically translating mechanical degrees of freedom coupled to an electrical degree of freedom. This model type captures the isolation mode and suspension mode, but not the coil mode. The smaller modal shakers being modeled often have a coil mode outside of typical testing ranges unless a relatively large mass is attached to the shaker. The model parameters were estimated using experimental modal analysis of the shaker and then using modal parameter estimation to estimate the mass and stiffnesses of each degree of freedom. Next the coupling coefficient of the shaker was determined by fixing the armature from moving and measuring the force output and dividing it by the current input to the shaker. Finally, the electrical parameters—resistance and inductance—were measured using an RLC meter. Martino and Harri then applied their model to virtual shaker testing, where the shaker, controller and DUT are all modeled, and a time-domain simulation of a vibration test is performed to assess its viability. While this method proves useful, it requires full time-step simulations of the test, modeling of the controller, and typically uses a finite element model of the DUT. This work only explored the shaker itself, with no DUT attached.

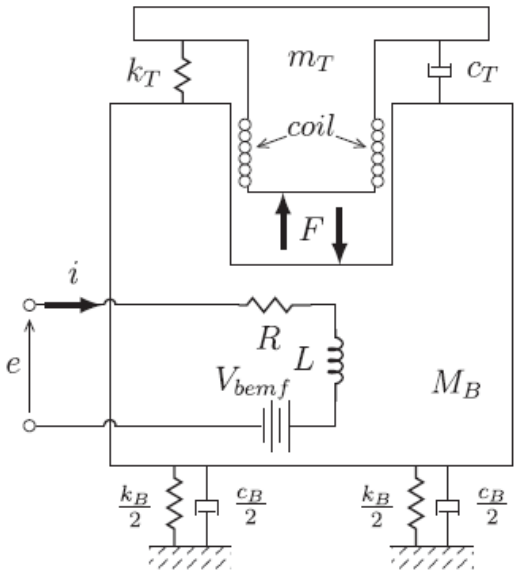


Figure 2.6.1 2-DoF shaker model capturing the isolation and suspension modes of the [10].

The majority of electrodynamic shaker models found in the literature are lumped parameter electro-mechanical models with three mechanical degrees of freedom, and one electrical degree of freedom. This model type was used by both Schultz [11] and Mayes [12] when modeling modal shakers with a test mass attached at the end of a stinger. Their models consisted of the body DOF, representing all the stationary components of the shaker, the armature DOF, representing the moving portion of the shaker, the stinger mass DOF, and finally the current in the shaker electronics. Schultz calibrated their model using a Monte Carlo random search to find the best model parameters to match data collected on the shaker itself. The data collected was measured using an accelerometer on the table and on the stinger mass, and a voltage divider and current probe to measure the electrical supply to the shaker. The chosen parameter set minimized the average of the L2 norm of the real and imaginary components of the shaker's impedance. Mayes performed two tests on the shaker, first utilizing a "zero-impedance" test with nothing attached to the armature, and then a "high-impedance" test where the armature was attached to a large steel

plate. The model parameters were then chosen based on the resonances of the shaker impedance curves from the two configurations. These models are useful in characterizing the smaller modal shakers and capturing the dynamics that are important to their application, but do not translate to larger shaker systems, which do not utilize stingers, and whose coil resonances are low enough to be in the frequency range of interest when testing.

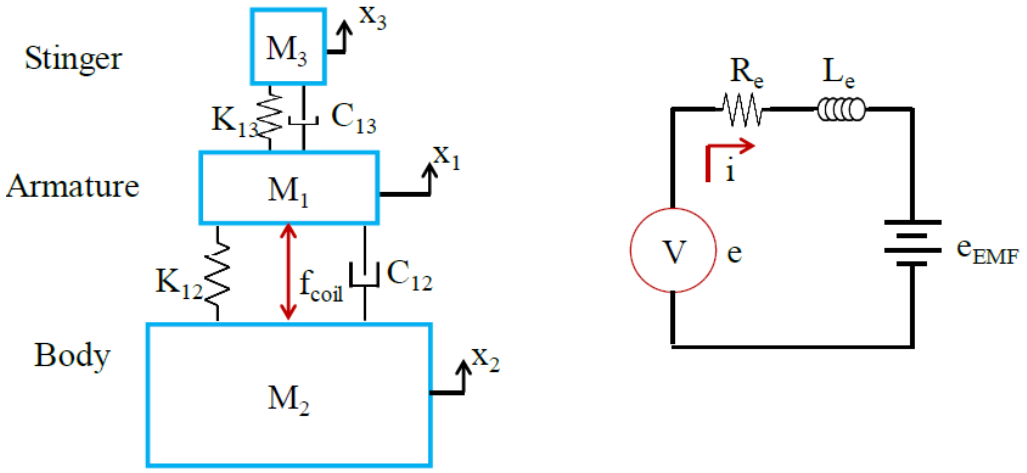


Figure 2.6.2 3-DoF shaker model with the body, armature, and stinger as the mechanical degrees of freedom [11].

When characterizing shakers for fixed-base testing, where the DUT is bolted to an armature table on the shaker, a different set of mechanical DOFs are commonly chosen. The body is still its own DOF, but the armature is treated as two elastically connected components, namely the table and the voice coil. This modeling approach directly captures the three modes discussed in the previous section and was used by Ricci et al [13] and Manzato et al [14]. These works also applied their models to virtual shaker testing. Both took a modal parameter estimation approach for model updating. These approaches utilized calibrated masses on the shaker table to measure the FRFs of the table acceleration over the input voltage and then performing the modal parameter estimation

on these FRFs. Acceleration was measured on the table, and the current and voltage supplied to the shaker were measured by a voltage divider and a current probe. The modes of the shaker were then fit individually and the modal parameters estimated used for the model.

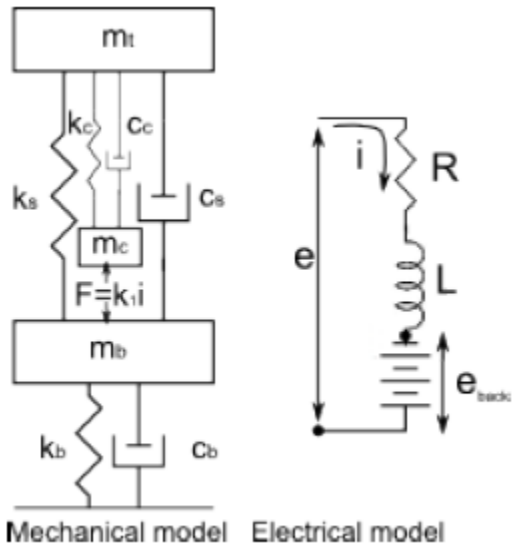


Figure 2.6.3 3-DoF shaker model with the body, armature table and voice coil as the mechanical degrees of freedom [14].

Hoffait et al [15] used a similar model to Ricci et al and Manzato et al but expanded the degrees of freedom of the three masses to also allow rotational motion in order to capture the out-of-axis motion of the shaker table. This results in 6 mechanical DOFs coupled to again a single electrical DOF. The mechanical DOFs were then connected not just by linear springs, but rotational springs as well. Impact testing was conducted on the shaker to characterize the dynamics of the system. Then, a manual fit of the model parameters was performed. From there an optimization method was used to minimize the least-square difference between the measured and computed frequency response functions (FRFs) to update the model.

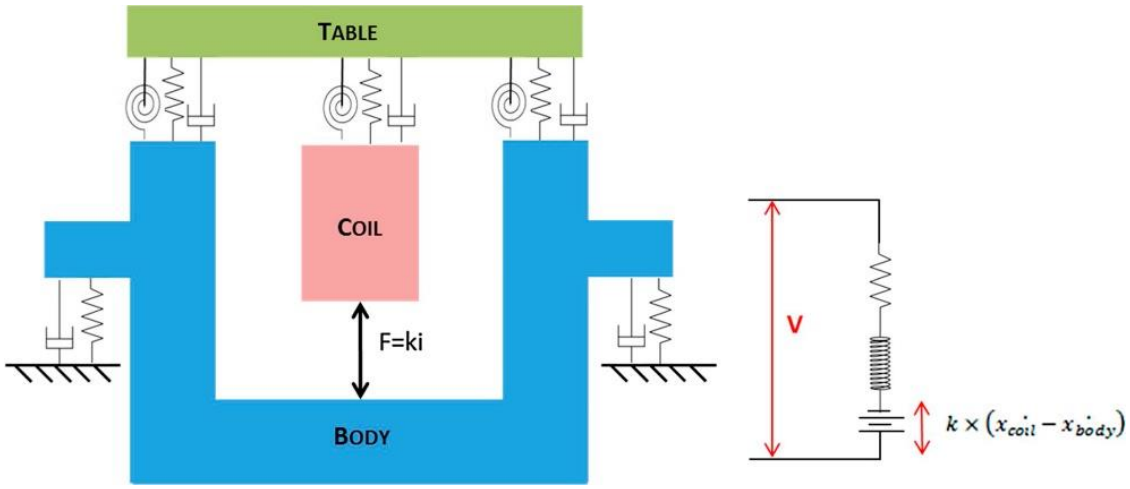


Figure 2.6.4 6-DoF shaker model that captures out of axis motion of the shaker using rotational degrees of freedom [15].

Others, such as Varoto and Oliveira [16] and McConnell [5] ignored the body DOF, as some shakers are rigidly attached to the ground or large seismic masses that cause the isolation mode to be very low frequency, below any frequency range of interest. Instead, a two mechanical DOF model was used, modeling just the armature table and voice coil as attached to the ground. These models capture only the suspension and coil modes. Importantly Varoto and Oliveira demonstrated the DUT and the shaker dynamics couple and interact with one another when a test is set up. This work confirms a need for a DUT model in order to fully understand and predict the outcome of a shock or vibration test.

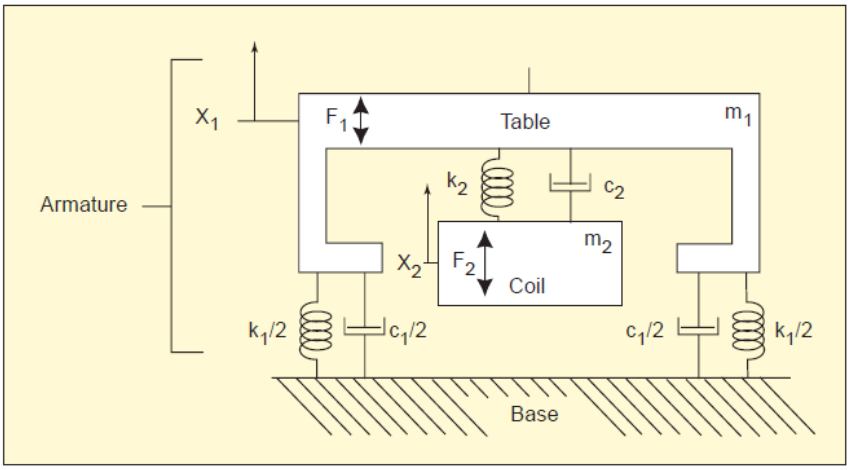


Figure 2.6.5 2-DoF model of the shaker armature, assuming the shaker body dynamics are negligible [16].

*2.6.2 Equivalent Electrical Models*

While electro-mechanical models of the shakers are the most common model types, some work approached shaker modeling as purely electrical systems. Tiwari et al [17] achieved this by utilizing the impedance analogy to develop a representative circuit of the shaker system that captured both the mechanical and electrical portions. This began as a lumped parameter mechanical model of the shaker which was converted to an equivalent circuit using the impedance analogy, and then coupled to the electrical system through the inductance of the voice coil. Four separate models were developed for each of the frequency regimes the shaker may operate in. Doing so allowed simplification of the models in the different ranges. The models were updated and validated in each of the ranges utilizing similar techniques to those mentioned before.

| | |
|---|---|
| $Bl$ | electromechanical coupling coefficient (force factor) |
| $C_b$ | compliance of isolation system |
| $C_c$ | compliance of armature assembly |
| $C_{ms}$ | compliance of armature suspension |
| $C_L$ | compliance of additional load |
| $L_E$ | inductance of armature coil |
| $M_b$ | mass of body of shaker |
| $M_c$ | mass of armature coil assembly of shaker |
| $M_L$ | mass of load |
| $M_{ms}$ | total mechanical mass $= M_t + M_c$ |
| $M_t$ | mass of table of shaker |
| $R_E$ | resistance of armature coil |
| $R_b$ | mechanical responsiveness of isolation system |
| $R_c$ | Mechanical responsiveness of armature assembly |
| $R_L$ | mechanical responsiveness of additional load |
| $R_{ms}$ | mechanical responsiveness of armature suspension |
| $Z$ | impedance across the terminals of the shaker coil |
| $Z_{mech}$ | mechanical impedance of the shaker |
| $\omega_{em}$ | angular frequency electro-mechanical resonance |
| $\omega_r$ | angular frequency corresponding to maximum real impedance |
| $\omega_s$ | angular frequency at suspension resonance |

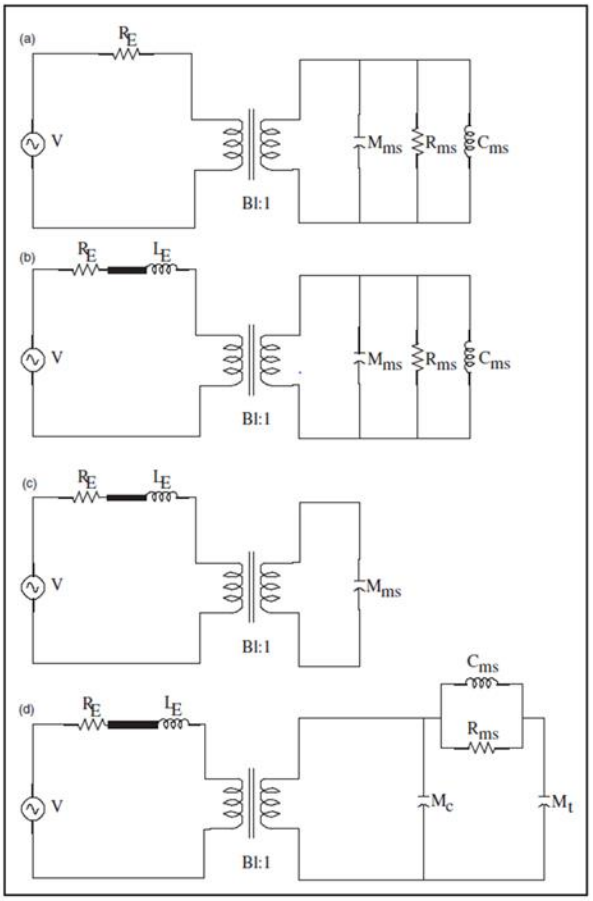


Figure 2.6.6 Equivalent electrical circuit shaker models for different frequency ranges of operation [17].

Lastly, Smallwood [18] utilized a two-port impedance model approach to modeling the shaker. The two-port network approach models the shaker as an impedance matrix which relates the voltage and current inputs supplied to the shaker to the acceleration and force outputs of the shaker. The acceleration was made analogous to the current and the voltage to the force. A 2x2 complex-valued matrix was developed based on measurements from the amplifier and accelerations on the shaker. This modeling approach is common in electrical modeling.

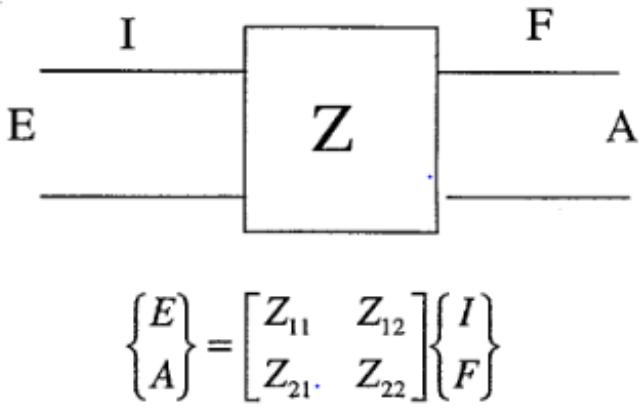


Figure 2.6.7 Two-port network model of a shaker [18].

## 2.7 Experimental Dynamic Substructuring Background

Dynamic substructuring is the set of techniques used by structural engineers to break down a large, complex dynamic system into subcomponents for higher fidelity modeling and analysis, while still preserving the overall dynamical properties of the system. These techniques are commonly applied to finite element analysis models to save time by modeling subcomponents separately and reassembling the results later. In experimental analysis it is used to test subcomponents separately and characterize local dynamics and assessing their contributions to system-level dynamics. One of the most powerful applications of dynamic substructuring is the ability to combine analytical and experimental analyses of subcomponents into a full model together [19]. This is the goal of dynamic substructuring for this project, to combine the analytical lumped parameter models discussed in the previous section with an experimentally developed model of a device under test to estimate the capability of a shaker system testing that DUT.

### *2.7.1 Substructuring Domains*

Dynamic substructuring can be represented and applied in many domains, most commonly the physical, modal, and frequency domains. In the physical domain, subcomponents are coupled together via their mass, stiffness, and damping components. In the modal domain these system matrices are utilized and considered in a modal basis, representing the responses of the structure. In the frequency domain, substructuring is performed using the frequency response functions (FRFs), and is the domain utilized for this work [19].

### *2.7.2 Frequency Based Substructuring*

Substructuring is not a new concept, and frequency-based-substructuring (FBS) has been explored and developed since the 1960s, when Rubin [20] represented mechanical structures through impedance and admittance matrices, showing these matrices could be used to simulate the joining of two mechanical systems. Crowley et al. [21] further developed the idea of using FRFs to simulate structural modifications when developing their "Structural Modification Using Response Functions" or SMURF method. Jetmundsen [22] then developed the classical form of FBS in 1988, which De Klerk et al. simplified [23] into the method used for this thesis, Lagrange-Multiplier Frequency-Based-Substructuring (LM-FBS). While mathematically equivalent, the use of two Boolean localization matrices in LM-FBS significantly reduces the complexity of "organizing" the degrees-of-freedom on each substructure when assembling [24].

FBS is commonly applied in the automotive, naval, and aerospace industries, where large systems are analyzed for noise and vibration. The full-scale structural dynamics of such large systems are difficult and expensive characterize. However, using experimental dynamic substructuring, individual components can be tested, analyzed, and coupled together to obtain full-

scale dynamics, as shown by Steenhoek et al [25]. Alternatively, smaller components can be experimentally characterized and coupled with large-scale models. This method has been applied for vehicle axle noise analysis [26], assessment of machinery isolation on ships [27], and for modifications to helicopter components [28].

### *2.7.3 Dynamic Equilibrium and Interface Conditions in the Frequency Domain*

FBS begins with the conditions of substructure assembly. This derivation is common in the dynamic substructuring literature, but [24] is a detailed source on the topic. Consider two substructures, R and S, shown in Figure 2.7.1.

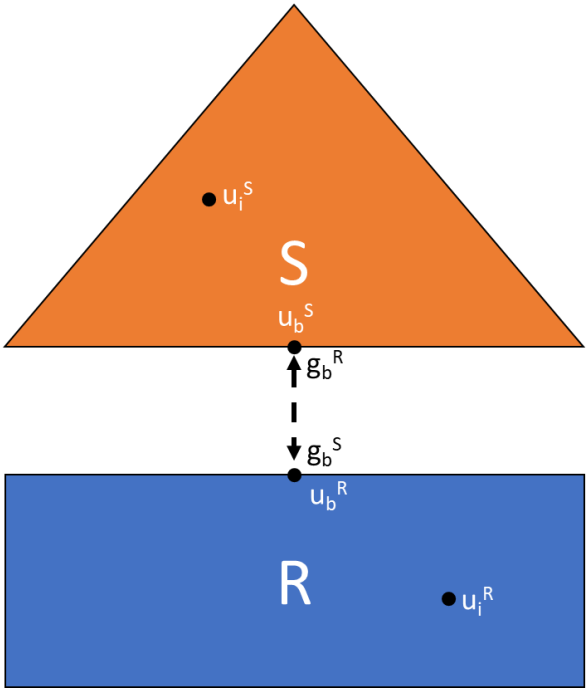


Figure 2.7.1 Assembly of two substructures R and S, at boundary nodes, $u_b$.

First, the dynamic equilibrium equation is considered,

$$\mathbf{Z}^{(s)}\bar{\mathbf{u}}^{(s)} = \bar{\mathbf{f}}^{(s)} + \bar{\mathbf{g}}^{(s)} \text{ for } s = 1,\ldots,N^{sub}, \tag{2.21}$$

where $\mathbf{Z}^{(s)}$ is the impedance, dynamic stiffness, or dynamic mass of the substructure. While any of these system matrices may be used, the responses used, $\mathbf{u}^{(s)}$ (displacement, velocity, or acceleration) must be consistent with the $\mathbf{Z}$ used. For this formulation let us assume $\mathbf{Z}^{(s)}$ is the dynamic stiffness matrix. Therefore $\mathbf{u}^{(s)}$ is the vector of displacement responses in the substructure to the sum of the external forces $\mathbf{f}^{(s)}$ and the internal forces $\mathbf{g}^{(s)}$ on the substructure. To couple one substructure s, to another substructure r, to create a single system, two interface conditions need to be satisfied: interface equilibrium and compatibility.

Interface equilibrium requires that the internal forces, or interface forces, between the two substructures must sum to zero when assembled,

$$\bar{\boldsymbol{g}}_{\boldsymbol{b}}^{(\boldsymbol{s})} + \bar{\boldsymbol{g}}_{\boldsymbol{b}}^{(\boldsymbol{r})} = \mathbf{0}\ \boldsymbol{on}\ \boldsymbol{\Gamma}^{(\boldsymbol{rs})}, \tag{2.22}$$

where $g_b^{(s)\ is}$ the interface force on the boundary DOFs on substructure s, $g_b^{(r)}$ is the interface force on the boundary DOFs on substructure r, and $\Gamma^{(rs)}$is the interface between the two substructures. The boundary DOF locations can be collected into a Boolean matrix $\mathbf{L}^{(s)T}$ with dimension $n \times n^s$ that combines the forces on either side of the interface. This matrix acts as a localization matrix which maps the local DOFs of the substructure to a unique set of global DOFs within the assembly. The interface equilibrium condition can then be written as

$$\sum_{\boldsymbol{s=1}}^{\boldsymbol{N^{sub}}} \boldsymbol{L}^{(\boldsymbol{s})^{\boldsymbol{T}}} \bar{\boldsymbol{g}}^{(\boldsymbol{s})} = \mathbf{0}. \tag{2.23}$$

The interface compatibility condition requires that the response at the DOFs on both sides of the interface must be equal,

$$\bar{\boldsymbol{u}}_{\boldsymbol{b}}^{(\boldsymbol{s})} - \bar{\boldsymbol{u}}_{\boldsymbol{b}}^{(\boldsymbol{r})} = \mathbf{0}\ \boldsymbol{on}\ \boldsymbol{\Gamma}^{(\boldsymbol{rs})}. \tag{2.24}$$

Like equation 2.22, here $u_b^{(s)}$ is the response on the boundary DOFs of substructure s, $u_b^{(r)}$ is the response of the boundary DOFs of substructure r, and $\Gamma^{(rs)}$ is the interface between the two

substructures. Similarly, the boundary DOF locations for the interface compatibility can be collected into a signed Boolean matrix $\mathbf{B}^{(s)}$. This matrix extracts the interface DOFs and gives them opposite signs on each side of the interface. Using this matrix, the interface compatibility condition can be written as

$$\sum_{s=1}^{N^{sub}} \boldsymbol{B}^{(s)}\overline{\boldsymbol{u}}^{(s)} = \mathbf{0}. \tag{2.25}$$

The set of equations laid out by equations 2.21, 2.23 and 2.25 defines the assembly of two substructures r, and s. This set of equations can be condensed into a block matrix form,

$$\begin{cases} \mathbf{Z}\overline{\mathbf{u}} = \bar{\mathbf{f}} + \bar{\mathbf{g}} \\ \mathbf{B}\overline{\mathbf{u}} = \mathbf{0} \\ \mathbf{L}^{\mathrm{T}}\bar{\mathbf{g}} = \mathbf{0} \end{cases}, \tag{2.26}$$

where $\mathbf{L}^{\mathrm{T}} = \left[\mathbf{L}^{(1)^{\mathrm{T}}}, \dots, \mathbf{L}^{(N_{sub})^{\mathrm{T}}}\right]$, $\mathbf{B} = \left[\mathbf{B}^{(1)}, \dots, \mathbf{B}^{(N_{sub})}\right]$

and $\mathbf{Z} = \begin{bmatrix} \mathbf{Z}^{1} & \cdots & \mathbf{0} \\ \vdots & \ddots & \vdots \\ \mathbf{0} & \cdots & \mathbf{Z}^{(N_{sub})} \end{bmatrix}$.

**B** and **L** have been defined in such a way that

$$\mathbf{L} = \mathrm{null}(\mathbf{B}), \text{therefore } \mathbf{BL} = \mathbf{0}. \tag{2.27}$$

This will be a useful relationship later.

The system of equations 2.26 has two sets of unknowns, the responses, **u,** or "primal unknowns" and the internal forces, **g**, or "dual unknowns." The set of unknowns can be reduced to simplify the problem by introducing unique interface displacements, referred to as "primal assembly," Alternatively, one can introduce interface forces that satisfy the interface equilibrium, referred to as "dual assembly."

*2.7.4 Primal Assembly*

The primal assembly method is commonly used in finite element modeling [19]. The Boolean matrix $L^T$ maps the DOFs of each substructure to a unique set of global DOFs. This matrix can then be used to transform the global responses $\mathbf{u_g}$ to the local response DOFs $\mathbf{u}$,

$$\mathbf{u} = \mathbf{L}\mathbf{u}_g. \tag{2.28}$$

Using the global response DOFs then defines the responses $\mathbf{u_g}$ as compatible. In the example of figure 2.7.1, it maps $u_b^S$ and $u_b^R$ to a single response DOF, $u_b$. We can then substitute this definition of $\mathbf{u}$ into the compatibility equation and find it is satisfied because of the relationship between $\mathbf{B}$ and $\mathbf{L}$ noted in Equation 2.27,

$$\mathbf{B}\mathbf{L}\mathbf{u}_g = \mathbf{0}\ \forall \mathbf{u}_g. \tag{2.29}$$

Using the global DOFs, the set of equations 2.26 can be simplified to just two equations,

$$\begin{cases} \mathbf{Z}\mathbf{L}\mathbf{u}_g = \bar{\mathbf{f}} + \bar{\mathbf{g}} \\ \mathbf{L}^{\mathbf{T}}\bar{\mathbf{g}} = \mathbf{0}. \end{cases} \tag{2.30}$$

Pre-multiplying the dynamic equilibrium by $\mathbf{L}^T$ in equation 2.30 then removes the internal forces term, as the equilibrium condition below defines $\mathbf{L}^T\mathbf{g} = \mathbf{0}$. The equation then simplifies to

$$\mathbf{L}^T\mathbf{Z}\mathbf{L}\mathbf{u}_g = \mathbf{L}^T\mathbf{f}. \tag{2.31}$$

$\mathbf{L}^T\mathbf{Z}\mathbf{L}$ is then the primal assembled impedance matrix of the coupled system.

*2.7.5 Dual Assembly*

The dual assembly approach lends itself to experimental substructuring because substructures are typically characterized by the FRFs of the system, which determine the component's response to excitations [19]. In dual assembly a set of interface forces, $\mathbf{g}$, are chosen such that the interface equilibrium condition is satisfied,

$$\mathbf{g} = -\mathbf{B}^{\mathrm{T}}\boldsymbol{l} \tag{2.32}$$

The $\boldsymbol{l}$ term in Equation 2.32 is the interface force intensities and are equal in number to the number of interface conditions. From equation 2.27 we know $\mathbf{BL} = \mathbf{0}$, therefore $\mathbf{L}^{\mathrm{T}}\mathbf{B}^{\mathrm{T}} = \mathbf{0}$, so the interface equilibrium will be satisfied by this definition of $\mathbf{g}$,

$$\mathbf{L}^{\mathbf{T}}\mathbf{B}^{\mathbf{T}}\boldsymbol{l} = \mathbf{0}\ \forall \boldsymbol{l}. \tag{2.33}$$

The dual assembly form of the problem is then

$$\begin{cases} \boldsymbol{Z}^{(s)}\overline{\boldsymbol{u}}^{(s)} = \overline{\boldsymbol{f}}^{(s)} - \boldsymbol{B}^{(s)^T}\boldsymbol{l}\ \textit{for s = 1,…,}\boldsymbol{N}^{\boldsymbol{sub}} \\ \sum_{\boldsymbol{s=1}}^{\boldsymbol{N}^{\boldsymbol{sub}}} \boldsymbol{B}^{(s)}\overline{\boldsymbol{u}}^{(s)} = \mathbf{0}\,, \end{cases} \tag{2.34}$$

which can be rewritten in block matrix form

$$\begin{bmatrix} \boldsymbol{Z} & \boldsymbol{B}^{\boldsymbol{T}} \\ \boldsymbol{B} & \mathbf{0} \end{bmatrix} \begin{bmatrix} \overline{\boldsymbol{u}} \\ \boldsymbol{l} \end{bmatrix} = \begin{bmatrix} \overline{\boldsymbol{f}} \\ \mathbf{0} \end{bmatrix}. \tag{2.35}$$

In this form, the $\boldsymbol{l}$ term can then be interpreted as the Lagrange multipliers associated with the equilibrium constraint.

*2.7.6 Lagrange Multiplier Frequency Based Substructuring*

The derivation of LM-FBS uses the dual assembly approach and begins with the dynamic equilibrium equation, the first in the set of equations 2.35. The equation can be rewritten to isolate the responses $\mathbf{u}$,

$$\overline{\mathbf{u}}^{(\mathrm{s})} = \mathbf{H}^{(\mathrm{s})}\left(\bar{\mathbf{f}}^{(\mathrm{s})} - \mathbf{B}^{(\mathrm{s})^{\mathrm{T}}}\boldsymbol{l}\right) \text{ where } \mathbf{H}^{(\mathrm{s})} = \mathbf{Z}^{(\mathrm{s})^{-1}}, \tag{2.36}$$

where $\mathbf{H}$ is the frequency response matrix of the substructure, s. The compatibility condition, the second equation in 2.35, may then be substituted into equation 2.36 and simplified,

$$\mathbf{B}\left(\mathbf{H}(\mathbf{f} - \mathbf{B}^{\mathrm{T}}\boldsymbol{l})\right) = \mathbf{0}$$

$$\mathbf{BHf} - \mathbf{BHB}^{\mathrm{T}}\boldsymbol{l} = \mathbf{0}$$

$$(\mathbf{BHB}^{\mathrm{T}})\boldsymbol{l} = \mathbf{BHf}. \tag{2.37}$$

Equation 2.37 can then be solved for ***l***,

$$\boldsymbol{l} = (\mathbf{BHB}^{\mathrm{T}})^{-1}\mathbf{BHf}. \tag{2.38}$$

This definition of ***l*** can be substituted into the dynamic equilibrium equation 2.36 and simplified again,

$$\mathbf{u} = \mathbf{H}(\mathbf{f} - \mathbf{B}^{\mathbf{T}}\boldsymbol{l})$$

$$\mathbf{u} = \mathbf{H}\left(\mathbf{f} - \mathbf{B}^{\mathbf{T}}((\mathbf{BHB}^{\mathbf{T}})^{-1}\mathbf{BHf})\right)$$

$$\mathbf{u} = \mathbf{Hf} - \mathbf{HB}^{\mathbf{T}}(\mathbf{BHB}^{\mathbf{T}})^{-1}\mathbf{BHf}$$

$$\mathbf{u} = (\mathbf{H} - \mathbf{HB}^{\mathbf{T}}(\mathbf{BHB}^{\mathbf{T}})^{-1}\mathbf{BH})\mathbf{f}. \tag{2.39}$$

Equation 2.39 defines the dynamic equilibrium of the fully coupled system. The FRF matrix $\mathbf{H}_{\text{dual}}$ can then be defined,

$$\mathbf{H}_{\mathbf{coupled,dual}} = \mathbf{H} - \mathbf{HB}^{\mathbf{T}}(\mathbf{BYB}^{\mathbf{T}})^{-1}\mathbf{BH}. \tag{2.40}$$

Equation 2.40 is the formula for LM-FBS and defines the FRF matrix of the fully coupled system. $\mathbf{H}_{\text{dual}}$ is defined for all the local DOFs on all the structures, and therefore contains redundant information at the interface DOFs.

### *2.7.7 Challenges to Frequency Based Substructuring*

While FBS offers a convenient means of characterizing large systems and directly utilizing experimental data, the method does have drawbacks. These include matrix inversions, propagation and magnification of measurement noise, the need to measure rotational degrees-of-freedom, and the need to measure directly at the interface degrees of freedom [19]. In the FBS calculation the matrix of FRFs is inverted, drastically magnifying measurement noise, and the matrix must be well-conditioned [29]. A common method of reducing FRF noise is by performing a modal

parameter estimation on the measured data and utilizing the synthesized FRFs from the results instead [30].

The rotational DOFs of a structure make up three quarters of the FRF matrix and therefore neglecting to include them can result in very poor estimates of the coupled dynamics of the assembly. Two common methods of addressing both the measurement location and rotational DOF issues are the virtual point method and the transmission simulator. The virtual point method uses measurements around the true connection point to extrapolate the dynamics to a virtual point between them. This method is an extension of the equivalent multi-point connection method (EMPC), which estimated connections by making three 3-DoF translational measurements on a connection surface and filtering the motion to the 6 rigid body modes of the surfaces, which were then used for coupling [31]. The virtual point transformation then further reduces the 9-DoF connections of EMPC to an estimate of the 6-DOF motion at a single connection point. These virtual points can then be made collocated for the two substructures being coupled to fully satisfy the assumptions of FBS [32].

While the virtual point transformation provides improvements to single point connections, it is still not feasible for surface connections, as it is difficult to excite even the three translational DOFs required on surfaces. Instead, the transmission simulator method provides a means of estimating the rotational DOFs and the surface contact of the connection and is typically applied to substructure coupling of a physical substructure to a finite element model. The transmission simulator is a physical fabrication of the interface between two substructures that is then modeled analytically. The transmission simulator is attached to the substructure of interest, and analytically attached to the model of interest. The motions of the model and the physical substructure are then constrained to be the same, coupling the two substructures together capturing the dynamics at all

connection locations, and estimating the rotational degrees of freedom from the analytical model. The mass and stiffness of the transmission simulator are then subtracted from the system to remove its effects [33]. Drawbacks of this method are the need to both model and fabricate the transmission simulator.

# 3.0 EXPERIMENTATION AND ANALYSES

## 3.1 Electrodynamic Shaker Model Development

A 4-DOF, lumped parameter model was chosen for modeling the electrodynamic shaker. This 4-DOF model appeared multiple times in the literature and proved to capture the dominant dynamics of most electrodynamic shaker systems. The model consists of three mechanical DOFs, the body of the shaker, the armature table, and the armature coil. These are elastically connected to one another with springs and dampers. The fourth DOF is the charge in the electrical component of the system. The circuit consists of a source EMF, the only input to the system, an inductor, and a resistor. The two models are connected by the force imparted on the mechanical system, between the body and the coil, and the corresponding back EMF on the electrical system, which is proportional to the relative velocity of the body and coil. A diagram of the model is shown in figure 3.1.1.

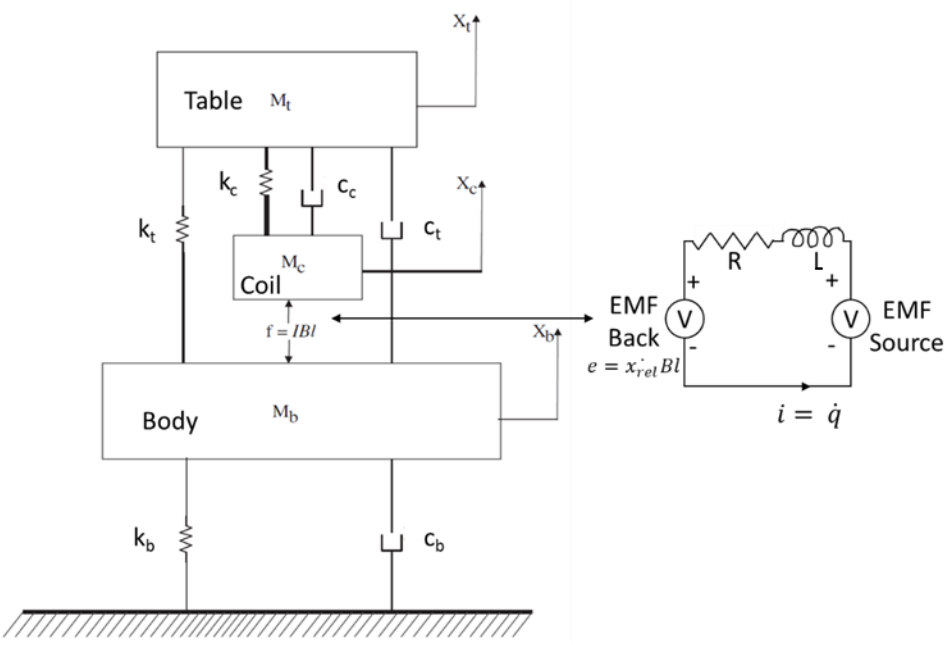


Figure 3.1.1 Shaker electromechanical model diagram.

### *3.1.1 Model Parameters*

The model consists of 12 parameters. The mechanical side contains the three masses, $m_b$, $m_t$ and $m_c$, the three springs, $k_b$, $k_t$, and $k_c$, and the three dampers $c_b$, $c_t$, $c_c$. The electrical model contains the resistance of the coil R, and the inductance, L. Lastly, the two systems are coupled together by the coupling factor Bl, which is replaced with a single constant K. This constant is only equal on both sides of the model if SI units are used. Of these 12 parameters, 5 were determined from the specification sheet provided by the shaker manufacturer and measurements made on the system. The shaker's body mass and armature mass, the sum of both the table and coil, as well as the flexure stiffness, $k_t$, were available. The resistance of the coil was measurable directly on the shaker input terminal. The remaining parameters must be estimated through measurements on the system itself.

### *3.1.2 Equations of Motion*

The end-use of this model is ultimately frequency-based substructuring, which couples together the frequency response functions of two different components to determine their coupled dynamics. Therefore, the FRFs of interest for this model must be calculated from it. First the equations of motion of the system were assembled based on the model. The mechanical system of equations can easily be assembled in matrix form,

$$\begin{bmatrix} m_b & 0 & 0 \\ 0 & m_t & 0 \\ 0 & 0 & m_c \end{bmatrix} \begin{Bmatrix} \ddot{u}_b \\ \ddot{u}_t \\ \ddot{u}_c \end{Bmatrix} + \begin{bmatrix} c_b + c_t & -c_t & 0 \\ -c_t & c_t + c_c & -c_c \\ 0 & -c_c & c_c \end{bmatrix} \begin{Bmatrix} \dot{u}_b \\ \dot{u}_t \\ \dot{u}_c \end{Bmatrix}$$

$$+ \begin{bmatrix} k + k_t & -k_t & 0 \\ -k_t & k_t + k_c & -k_c \\ 0 & -k_c & k_c \end{bmatrix} \begin{Bmatrix} u_b \\ u_t \\ u_c \end{Bmatrix} = \begin{Bmatrix} f_b \\ f_t \\ f_c \end{Bmatrix}. \tag{3.1}$$

In this system of equations, the forces, f, are shown but will be zero in practice. Now the electrical equation can be written, as it is just a single degree of freedom. Because the mechanical system is written in terms of displacement, it makes most sense to write the electrical equation in terms of charge, q, so the time-derivatives of the two systems will be consistent when combined,

$$L\ddot{q} + R\dot{q} = E. \tag{3.2}$$

In this equation, the input is the source voltage E, and will be the only input to the full system.

Now the two equations may be coupled together using the coupling coefficient K,

$$\begin{bmatrix} m_b & 0 & 0 & 0 \\ 0 & m_t & 0 & 0 \\ 0 & 0 & m_c & 0 \\ 0 & 0 & 0 & L \end{bmatrix} \begin{Bmatrix} \ddot{u}_b \\ \ddot{u}_t \\ u_c \\ \ddot{q} \end{Bmatrix} + \begin{bmatrix} c_b + c_t & -c_t & 0 & -K \\ -c_t & c_t + c_c & -c_c & 0 \\ 0 & -c_c & c_c & K \\ K & 0 & -K & R \end{bmatrix} \begin{Bmatrix} \dot{u}_b \\ \dot{u}_t \\ u_c \\ \dot{q} \end{Bmatrix} + \begin{bmatrix} k_b + k_t & -k_t & 0 & 0 \\ -k_t & k_t + k_c & -k_c & 0 \\ 0 & -k_c & k_c & 0 \\ 0 & 0 & 0 & 0 \end{bmatrix} \begin{Bmatrix} u_b \\ u_t \\ u_c \\ q \end{Bmatrix} = \begin{Bmatrix} f_b \\ f_t \\ f_c \\ E \end{Bmatrix}. \tag{3.3}$$

If the matrices are then denoted $\tilde{\mathbf{M}}$, $\tilde{\mathbf{C}}$, and $\tilde{\mathbf{K}}$ respectively, the vector of response DoFs denoted **u**, and the vector of input forces be **f**, the system can efficiently be written in a familiar form,

$$\tilde{\mathbf{M}}\ddot{\mathbf{u}} + \tilde{\mathbf{C}}\dot{\mathbf{u}} + \tilde{\mathbf{K}}\mathbf{u} = \tilde{\mathbf{f}}. \tag{3.4}$$

*3.1.3 Frequency Response Functions*

From equation 3.3 and its restatement as equation 3.4, the FRFs of the system can be easily calculated using the direct frequency response method [11],

$$\mathbf{H} = \left(-\omega^2\tilde{\mathbf{M}} + \mathrm{j}\omega\tilde{\mathbf{C}} + \tilde{\mathbf{K}}\right)^{-1}. \tag{3.5}$$

Where **H** is the frequency response function matrix of the full system. **H** is calculated on a frequency line basis, with ω being the frequency, in radians per second, at that line. The result is

4x4xn matrix, where n is the number of frequency lines calculated. As stated previously, there are no input forces on the mechanical degrees of freedom, so only the fourth column of FRFs is needed, which are the responses to a voltage input, E. More specifically, the relationship between the mechanical response of the table to the electrical input to the shaker system is desired. This is the FRF in row 2, column 4 but must first be differentiated twice from its current form, receptance, to the accelerance form which will match measured acceleration data collected for updating the model. Also of interest is the response of the table to the current input to the system and the electrical impedance. The impedance is the inverse of the row 4 column 4 FRF, while the acceleration-current FRF will be the ratio of the row 2, column 4 FRF and the row 4, column 4 FRF.

The three FRFs of interest are affected by each of the parameters in the model. A parameter sensitivity study was performed to understand how changes in these parameters manifest in the FRFs. A baseline value was chosen for each of the parameters and held constant throughout. Then, one parameter at a time was subjected to an upward and downward perturbation. Plots of the baseline and each perturbation were made to visualize the effects the parameter has on the model results. Figure 3.1.2 shows an example of the effects of changing the mass on the table. After completing the perturbations for each of the parameters, the effects were assembled into Table 3.1, as well as the expected source for that parameter value. While the effects on all three FRFs were viewed, the effects in Table 3.1 focus on the shaker's impedance.

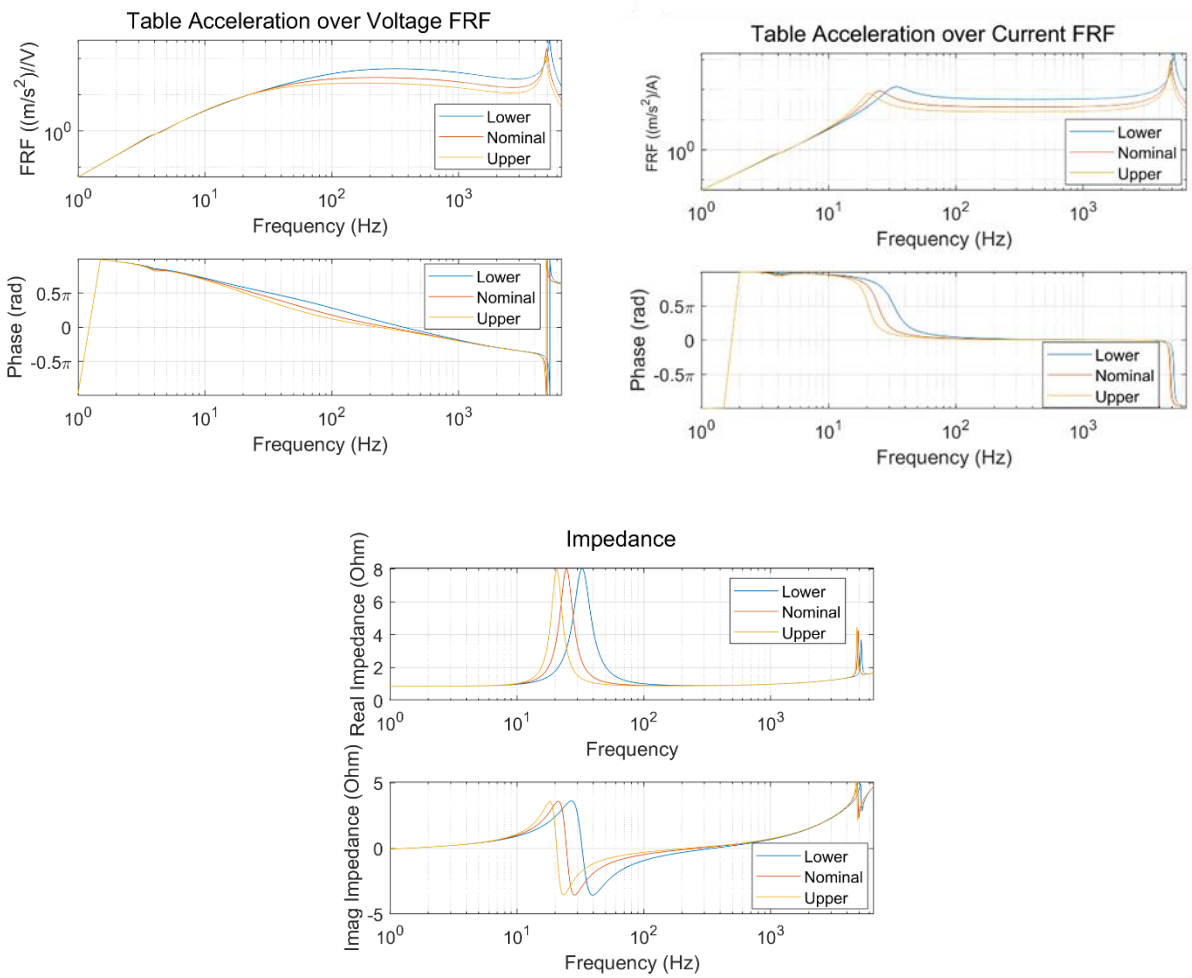


Figure 3.1.2 Effects of changing the table mass on the three FRFs of interest.

Table 3.1.1 Model parameter sensitivities

| Parameter | Source | Effect on impedance |
|---|---|---|
| $M_b$ – Shaker body mass | Spec Sheet | Shift frequency of isolation mode |
| $M_t$ – Table mass | Spec Sheet, Estimate<br>$M_t + M_c = M_{armature}$ | Shift frequency of isolation mode and suspension mode |
| $M_c$ – Coil mass | Spec Sheet, Estimate<br>$M_t + M_c = M_{armature}$ | Shifts frequency of isolation mode and coil mode |
| $C_b$ – Isolation mount damping | Estimate | Shifts amplitude of isolation mode |
| $C_t$ – Flexure damping | Estimate | Shifts amplitude of suspension mode |
| $C_c$ – Coil damping | Estimate | Shifts amplitude of suspension mode and coil mode |
| $K_b$ – Isolation mount stiffness | Estimate | Shifts frequency of isolation mode |
| $K_t$ – Flexure Stiffness | Spec Sheet | Shifts frequency of suspension mode |
| $K_c$ – Coil stiffness | Estimate | Shifts frequency of suspension mode, slightly coil mode |
| R – Coil resistance | Measure | Shifts overall amplitude slightly, significantly shifts coil mode amplitude. |
| L – Coil inductance | Estimate | Shifts coil mode frequency |

### *3.1.4 Shaker Model Validation Test setup*

The model developed must be validated using data from the shaker itself. This is especially important, as only 5 of the 12 parameters are known before updating. To capture the behavior of the shaker, a test was setup to measure the three FRFs of interest. The shaker characterized is a Modal Shop (TMS) K2075E dual-purpose 75 lbf shaker. This small shaker has an armature table and voice coil similar to large shaker systems used for ground and flight testing. Two triaxial accelerometers were placed on the shaker, with one on the armature table and one on the body of the shaker. Figure 3.1.3 shows the setup of the test. The body accelerometer was placed on the underside of the black housing of the shaker but is obscured by the slip table trunnion in the figure. The amplifier's built-in current monitor was used to measure the current supplied to the shaker,

and a voltage probe was attached to the amplifier output terminal to measure the voltage. In addition to the voltage from the amplifier, the drive voltage from the DAQ was measured. This setup captures nearly all the degrees of freedom in the model, but the armature coil is inaccessible for direct measurement.

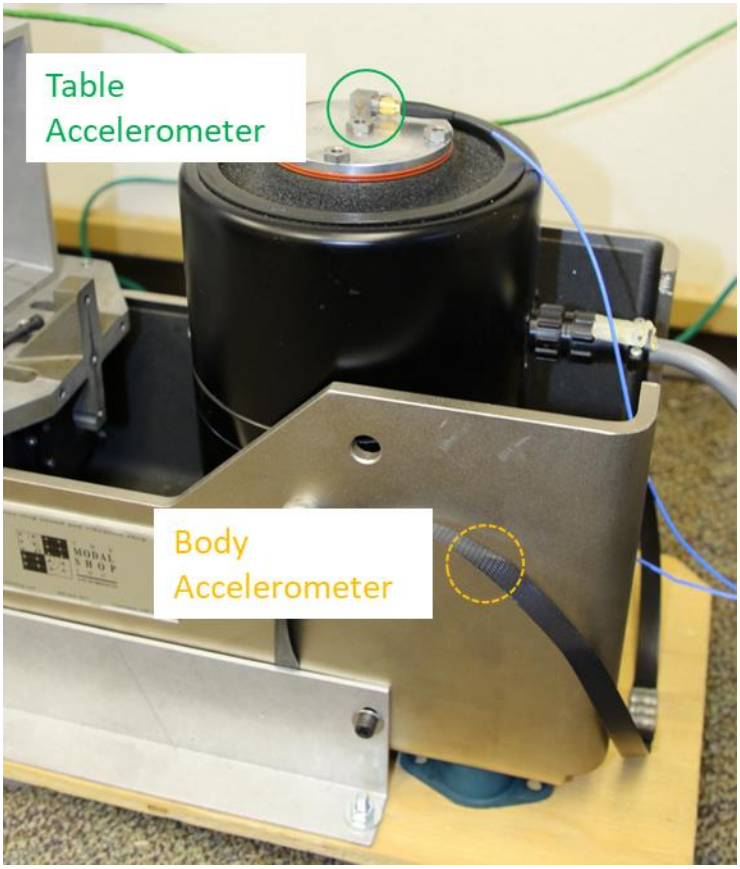


Figure 3.1.3 Shaker model validation test setup. The body accelerometer is behind the slip table housing.

The test profile used was a flat 1 gRMS PSD from 1 Hz to 6500Hz with a 1 Hz frequency spacing to characterize the full range of the shaker's dynamics. The full level was run for 90 seconds. The frequency limits were based on the limitations of the equipment used, the expected dynamics of the system, and the controllability of the profile. The test was controlled using the

Siemens LMS Testlab 2021.1 software's random control module. The test was run both open loop and closed loop to observe any effects of the controller on the FRFs. For the closed loop control the test was controlled on the Z-axis of the table accelerometer. The data was collected in the time-domain using a sample rate of 25.6 kHz.

### *3.1.5 Test Results*

The results from the characterization test closely matched the shape of the expected curves from the literature. The three FRFs were calculated from the time data collected using a two second Hanning window with a 50% overlap. Figures 3.1.4 through 3.1.6 show the results of the analysis. The shaker impedance, which is the measured voltage over the measured current across the frequency range, is shown in the real-imaginary form, while the other two FRFs are displayed in magnitude-phase form. The impedance sees virtually no difference between using an open loop or a closed loop control. The other two FRFs show a slight difference in magnitude just at the 1 Hz frequency line. This difference is accentuated by the log-log format used, and there is a maximum of 5% difference between the two signals at all other frequencies. These results show that the control algorithm does not significantly influence these FRFs. Two modes, the suspension and coil modes, are clearly visible on the plots, but the isolation mode is not. It is possible that either the mode is out of the range excited or does not have sufficient amplitude to be viewed. In either case, this indicates the model may be successful without including the body degree of freedom.

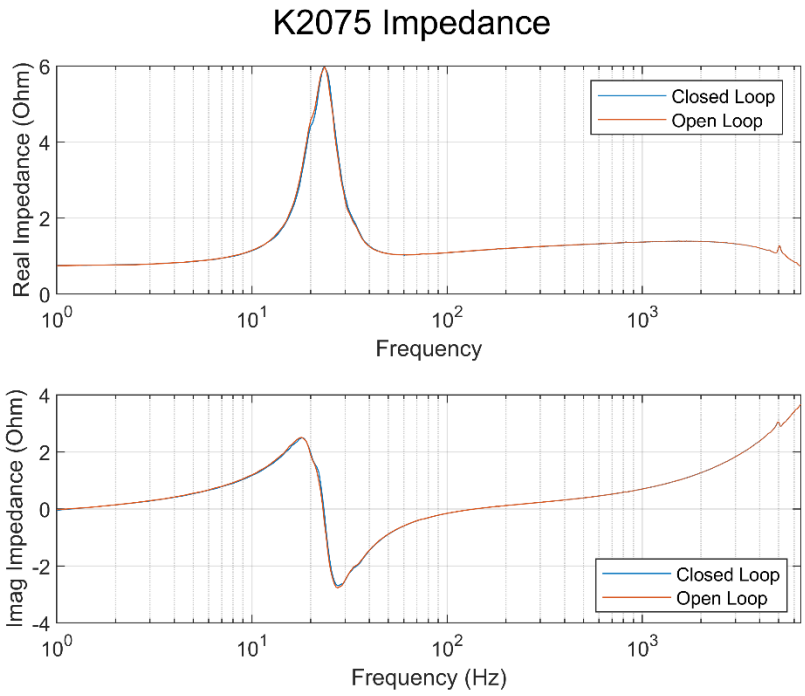


Figure 3.1.4 Shaker measured impedance.

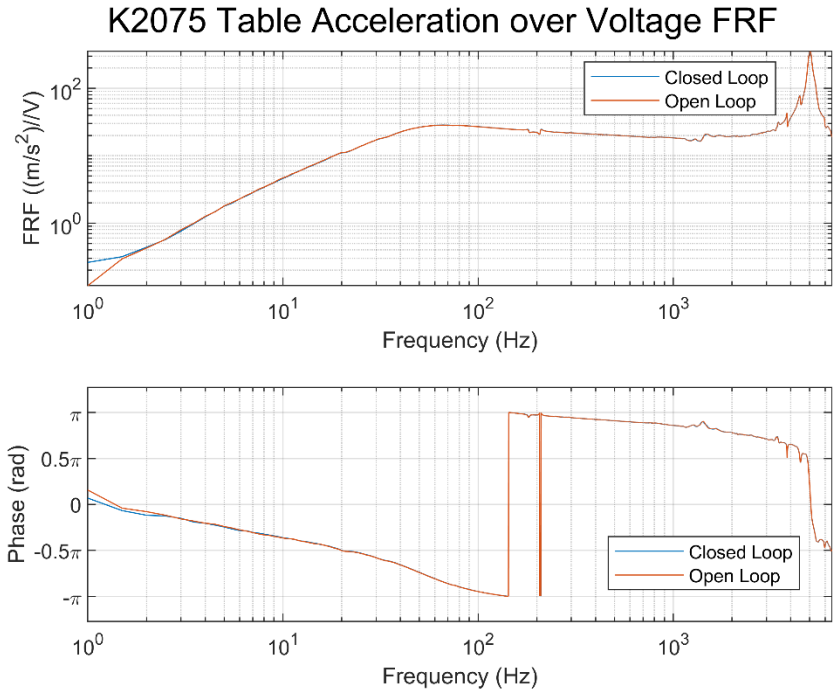


Figure 3.1.5 Shaker measured acceleration over voltage FRF.

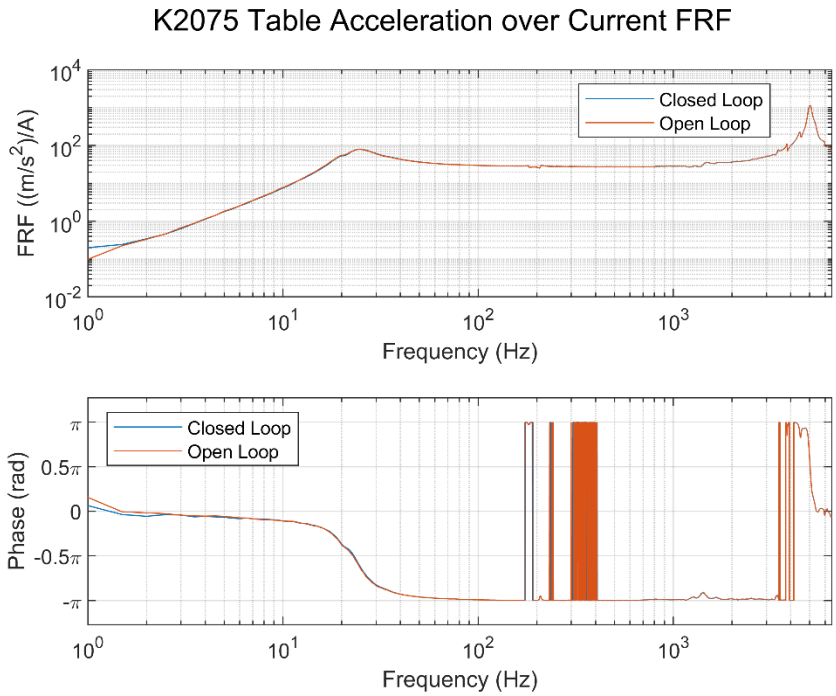


Figure 3.1.6 Shaker measured acceleration over current FRF.

*3.1.6 Model Updating*

The data collected in the characterization test was then used for updating the model. First the model was updated by hand to get an approximate fit of the data and provide a starting point for an optimization that would determine the final fit of the model. Using the results of the parameter sensitivity study, model parameters were chosen by trial and error and compared to the data. In accordance with the literature, an imaginary component was added to the inductance, as some amplifiers display a fixed phase difference between the current and voltage. This phase difference results in a real component of the impedance that increases proportional with frequency. While making the inductance complex compensates for this, it is not indicative of the physical phenomenon occurring [11][12]. Figures 3.1.7 through 3.1.9 show the manual fit compared to the data from the test, and Table 3.2 contains the parameter values chosen.

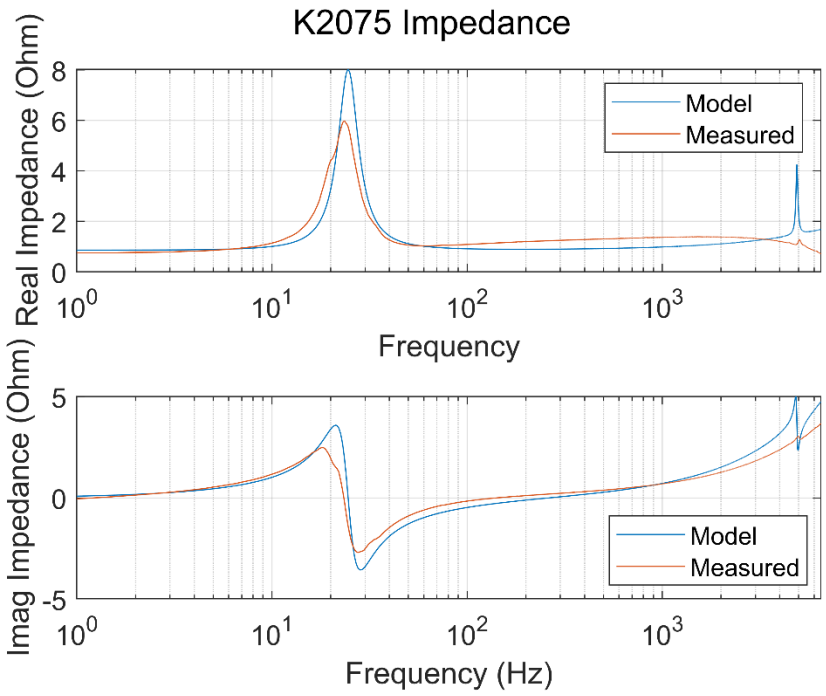


Figure 3.1.7 Comparison of the modelled and measured impedance of the small shaker.

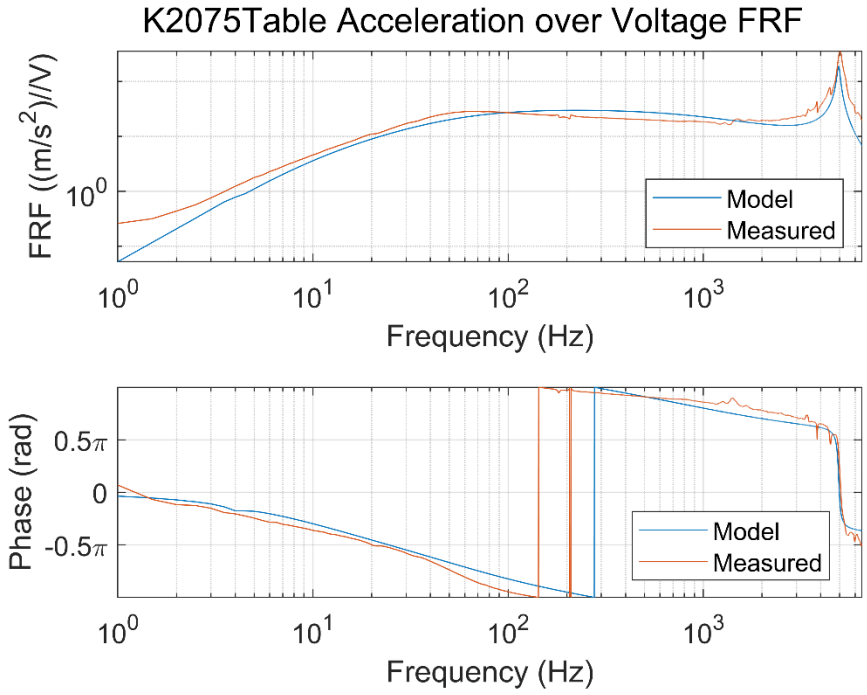


Figure 3.1.8 Comparison of the modelled and measured table acceleration over amplifier voltage FRF of the small shaker.

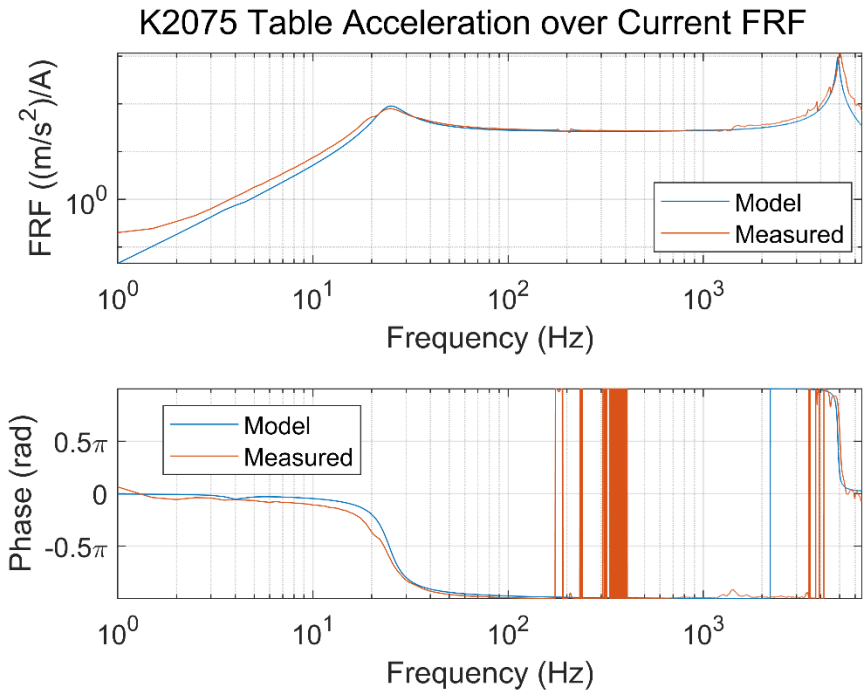


Figure 3.1.9 Comparison of the modelled and measured table acceleration over amplifier current FRF of the small shaker.

The hand fit model was then used as the initial state for the optimization to make the final model fit. MATLAB's *fmincon* algorithm was used for the optimization. *fmincon* is a gradient-based nonlinear constrained optimization algorithm. The algorithm assumes that the objective function used as well as its derivative are continuous. The objective function used was a weighted sum of the root mean square (RMS) errors of the real and imaginary parts of each FRF across all frequency lines,

$$e_{FRF} = \sqrt{\frac{\sum_{n=1}^{N}\sum\left(real(h_{n,model}) - real(h_{n,measured})\right)^2}{N}} + \sqrt{\frac{\sum_{n=1}^{N}\sum\left(imag(h_{n,model}) - real(h_{n,measured})\right)^2}{N}}, \tag{3.6}$$

$$e_{model} = a_1 e_{Impedance} + a_2 e_{Accel-Voltage} + a_3 e_{Accel-Current}. \quad (3.7)$$

In these equations $h_n$ is the value of the FRF at the $n^{th}$ frequency line, N is the total number of frequency lines, and $a_i$ is the weight assigned to the RMS error of that FRF. The default step, constraint, and optimality tolerances were used. The five model parameters that could be determined from the specification sheet of the shaker and measurements (body mass, table mass, coil mass, flexure stiffness, and resistance) were held fixed while the remaining 8 parameters were allowed to vary. The only constraint used was that parameters must be nonnegative. Weights were applied to normalize the magnitudes of the FRFs. Without them, the acceleration-current FRF dominates the error calculation purely because of its magnitude. While relative error may also be an option, the zero crossings in the imaginary parts of the FRFs tend to dominate the calculation, resulting in a poor fit. Table 3.2 also shows the parameter values determined from the optimization, and figures 3.1.10 through 3.1.12 compare the calculated FRFs from these parameters to the measured data. The optimization algorithm reduced the error in the model by only 5%. Most of the model parameters were not drastically changed. The body and damping stiffnesses showed almost no change at all. This is likely because the isolation mode is not clearly seen in the measured data and had little impact on the value of the objective function. In addition, the imaginary portion of the inductance approaches machine precision zero, indicating the amplifier used did not display the phase-difference issue seen in the literature. Lastly the coil stiffness showed very little change, likely because of its large magnitude, and confounding influences from the coupling coefficient.

Table 3.1.2 Chosen model parameters

| Parameter | Hand Fit Value | Updated Value | Units |
|---|---|---|---|
| Body Mass | 15.55 | 15.55 (fixed) | kg |
| Table Mass | 0.37 | 0.37 (fixed) | kg |
| Coil Mass | 0.08 | 0.08 (fixed) | kg |
| Body Damping | 100 | 99.99 | N/(m/s) |
| Flexure Damping | 20 | 23.22 | N/(m/s) |
| Coil Damping | 40 | 43.90 | N/(m/s) |
| Body Stiffness | 10000 | 10000 | N/m |
| Flexure Stiffness | 10500 | 10500 (fixed) | N/m |
| Coil Stiffness | 6.500e7 | 6.5000e7 | N/m |
| Resistance | 1.00 | 1.00 (fixed) | Ω |
| Real (Inductance) | 1.200E-04 | 1.195E-04 | H |
| Imag (Inductance) | 2.00E-05 | 5.010E-10 | H |
| Coupling Coefficient | 12 | 15.11 | - |

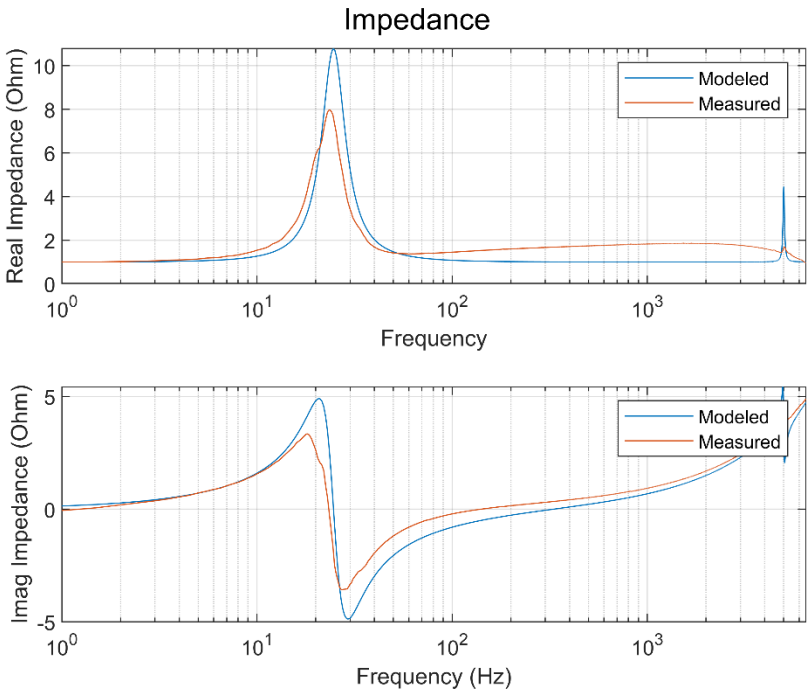


Figure 3.1.10 Comparison of the updated model and measured impedance of the small shaker.

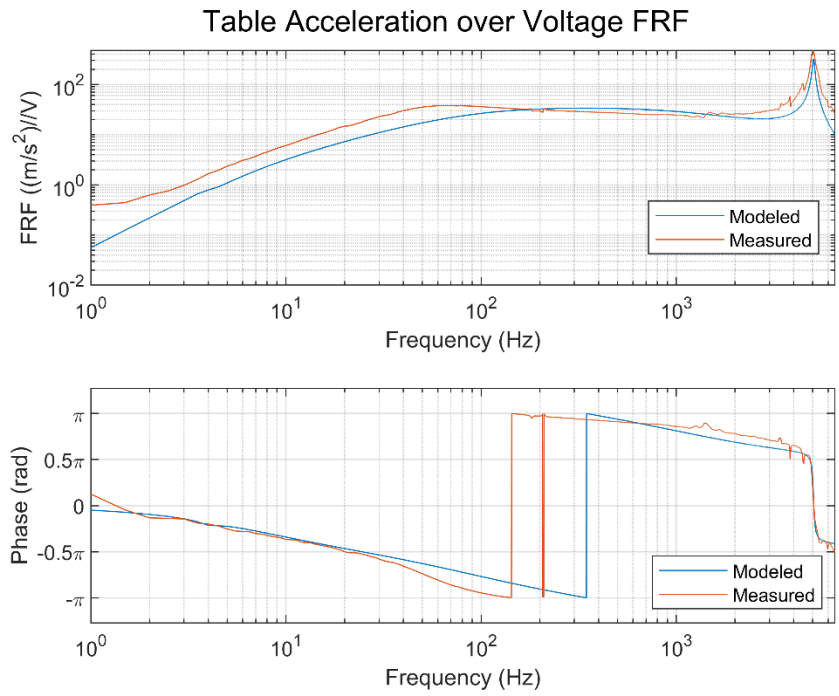


Figure 3.1.11 Comparison of the updated model and measured table acceleration over amplifier voltage FRF of the small shaker.

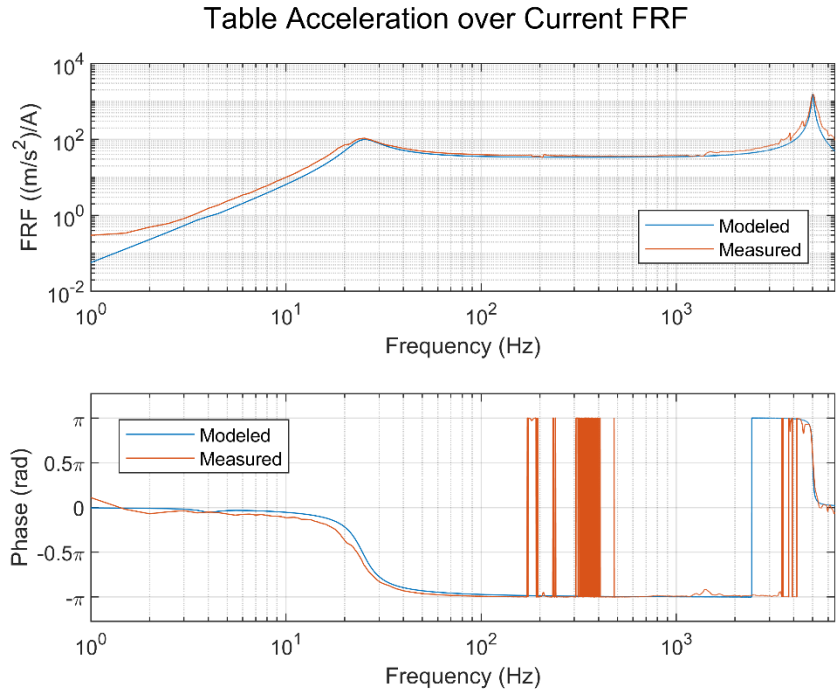


Figure 3.1.12 Comparison of the updated model and measured table acceleration over amplifier current FRF of the small shaker.

## 3.2 Experimental Dynamic Substructuring Implementation

A generic DUT was needed for assessing the effectiveness of using experimental dynamic substructuring for shaker capability estimation. The base of the Box Assembly and Removable Component (BARC) was chosen as the DUT. The BARC is a common challenge testbed used within the structural dynamics and dynamic environments testing community. The base of the BARC, i.e., without the removable component, was used because it does not contain any bolted joints, which are dynamically complex and difficult to characterize. Figure 3.2.1 shows the BARC base that was used.

### *3.2.1 Substructure Modal Testing*

A multi-reference impact test (MRIT) was performed to develop a modal model of the BARC base. The test was performed with the BARC suspended from a modal test stand using fishing wire to approximate a free-free boundary condition. A combination of uniaxial and triaxial accelerometers were used, totaling twelve sensors and 24 reference channels. A modal impact hammer was used for excitation. All data was collected using a Siemens LMS SCADAS Mobile DAQ and Siemens Simcenter Testlab 2021.1 Impact Testing software. Sensor channel ranges were selected to maximize the input to the ADC. A bandwidth of 8192 Hz with 16384 spectral lines was used, resulting in a two second acquisition window. The structure is very lightly damped and continued to resonate after the acquisition window ended, causing low-frequency leakage, so a 30% exponential decay window was applied to the data collected. A 5% force-exponential window was used on the input. Five averages were collected for each FRF. Figure 3.2.1 shows the test setup.

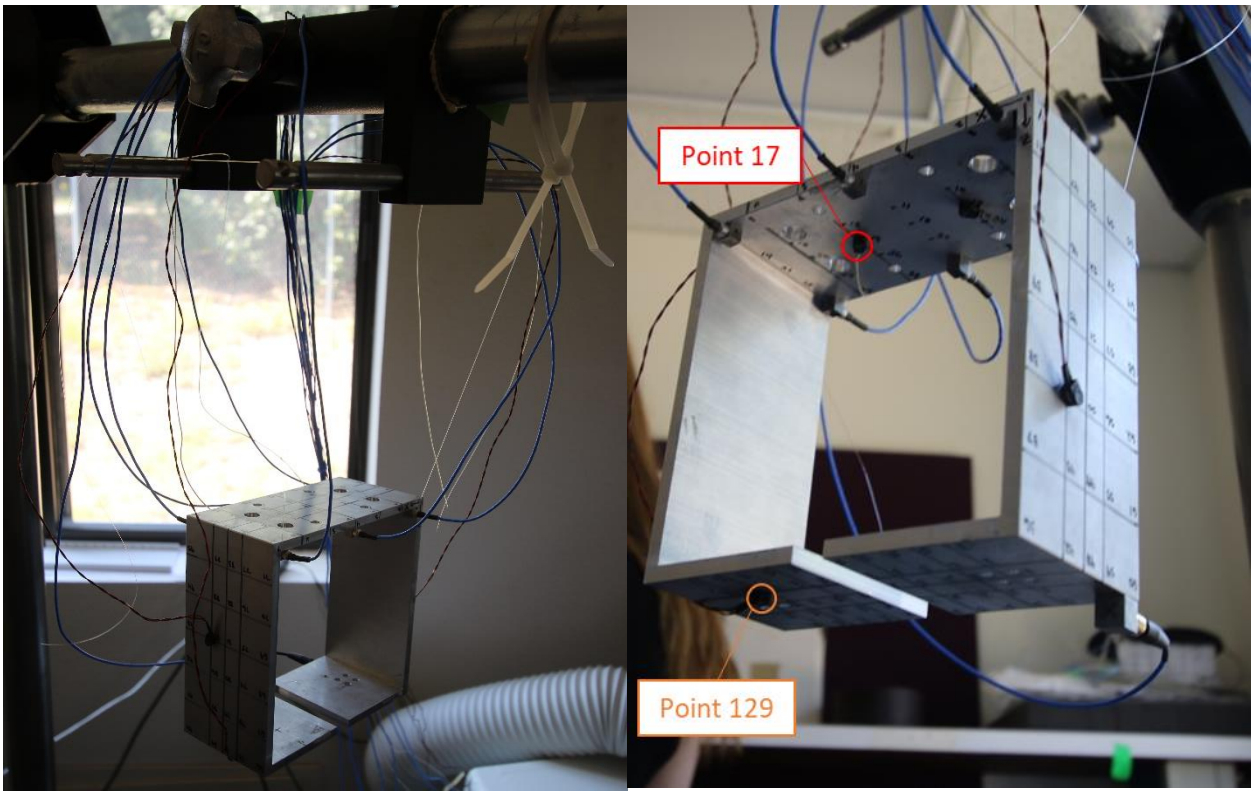


Figure 3.2.1 Modal impact test setup.

A driving point measurement is needed at each of the connection points for substructure coupling. In addition, each “point of interest” anywhere else on the structure also requires a driving point. These points could be potential control points that must be evaluated for estimating shaker capability. The results of the driving point measurements are a 24×24×16384 FRF matrix that was used for modal parameter estimation.

Modal parameter estimation was performed using the orthogonal polyreference, or OPoly, algorithm in the third-party MATLAB toolbox, IMAT 7.9.0, developed by ATA Engineering. First the full range of interest, from 1 Hz up to 6500 Hz was attempted for modal parameter estimation. However, the parameter estimation algorithm struggled with fitting such a large frequency range. This difficulty is likely because the test conducted did not well characterize the rigid body modes which occurred between 0 Hz and 10 Hz. Additionally, the input spectrum achieved by the hammer

begins to roll off significantly after 6000 Hz. Instead, a shorter range was fit, from 1 Hz to 2800 Hz, which spanned from the rigid body modes up to the fifteenth elastic mode. Figure 3.2.2 shows a sample FRF from point number 17, located offset from the center of the bottom plate on the BARC base and was used as a connection point in the substructuring analysis. Figure 3.2.3 shows a sample FRF from point number 129, located on the top of the BARC base structure, and used as a "point of interest."

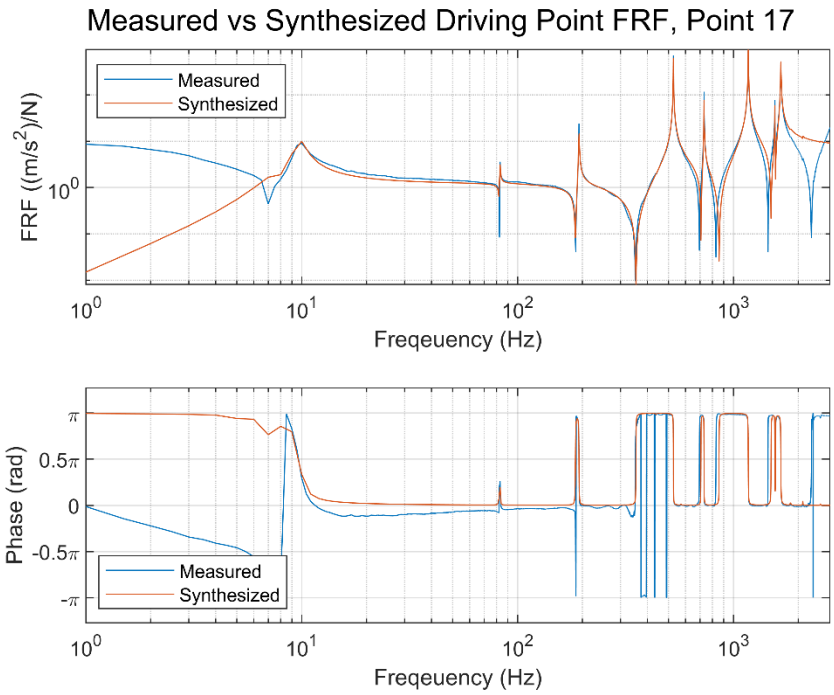


Figure 3.2.2 FRF measured and synthesized from modal parameters at point 17 of the BARC base.

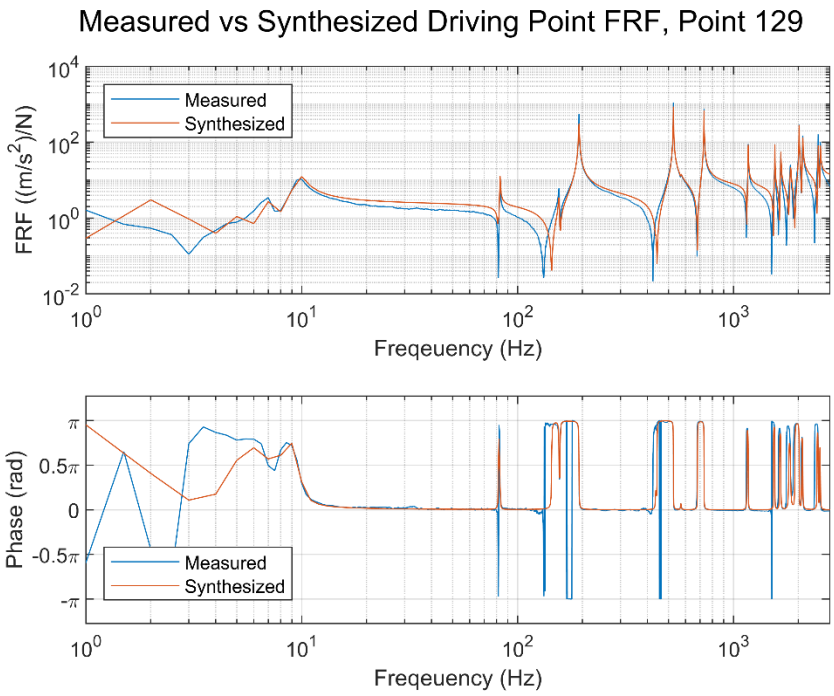


Figure 3.2.3 FRF measured and synthesized from modal parameters at point 129 of the BARC base.

The modal parameter estimation best fits the data below 1000 Hz but is an adequate fit overall. In both locations the frequencies of the antiresonances are overestimated and their magnitudes underestimated. Point 17 sits along the width centerline of the BARC base, so fewer modes are seen, as it cannot measure torsional modes, or modes occurring on the upper faces. Point 129 sees 14 of the 15 elastic modes fit.

### *3.2.2 Substructuring Analysis*

The experimental model of the BARC base was coupled to the analytical model of the shaker using Equation 2.40. The synthesized FRFs of the BARC base are the data used for the substructure coupling analysis, because they are analytically derived from the estimated modal parameters and are less noisy. Similarly, the FRFs calculated from the model of the small shaker

are used. Points 17 and 19 were chosen as the coupling points on the BARC base and were coupled with the table DOF of the shaker model. This creates two interface conditions.

First the B matrix is developed for each substructure,

$$\mathbf{B}^{(\text{shaker})} = \begin{bmatrix} 0 & 1 & 0 & 0 \\ 0 & 1 & 0 & 0 \end{bmatrix}, \mathbf{B}^{(\text{BARC})} = \begin{bmatrix} 0 & \dots & -1 & 0 & \dots & 0 \\ 0 & \dots & 0 & -1 & \dots & 0 \end{bmatrix}.$$

The nonzero elements of the BARC **B** matrix are in columns 9 and 10. The two matrices are then concatenated horizontally. Next the FRF matrix, $\mathbf{H}_{\text{uncoup}}$, is assembled block-wise, similarly to the **B** matrix,

$$\mathbf{H} = \begin{bmatrix} \mathbf{H}_{\text{shaker}} & \mathbf{0} \\ \mathbf{0} & \mathbf{H}_{\text{BARC}} \end{bmatrix}.$$

The **B** and **H** here are put into Equation 2.40, and the coupled FRF matrix $\mathbf{H}_{\text{coup}}$ is then calculated on a frequency line basis. The frequency range of the modal parameter estimation, 1 Hz to 2800 Hz, with a 1 Hz spacing was used. The results of the analysis are seen in Figures 3.2.8 through 3.2.12.

### *3.2.3 DUT-Shaker Coupling Validation Test*

The substructuring analysis must be experimentally validated, so a random vibration test of the BARC base attached to the shaker was conducted. This test utilized the same instrumentation setup on the BARC base as in the modal test, but also measured the current and voltage supplied by the amplifier to the shaker, like the test conducted for validating the shaker model. The test was run using the random vibration control module of Siemens Simcenter Testlab 2021.1. The test specification was a flat 1.5 gRMS PSD from 10 Hz to 6000 Hz with a 2 Hz frequency resolution. The full level was run for 90 seconds. The test was average controlled from Points 17 and 19, and a sample rate of 25.6 kHz was used. Figure 3.2.4 shows a setup of the test.

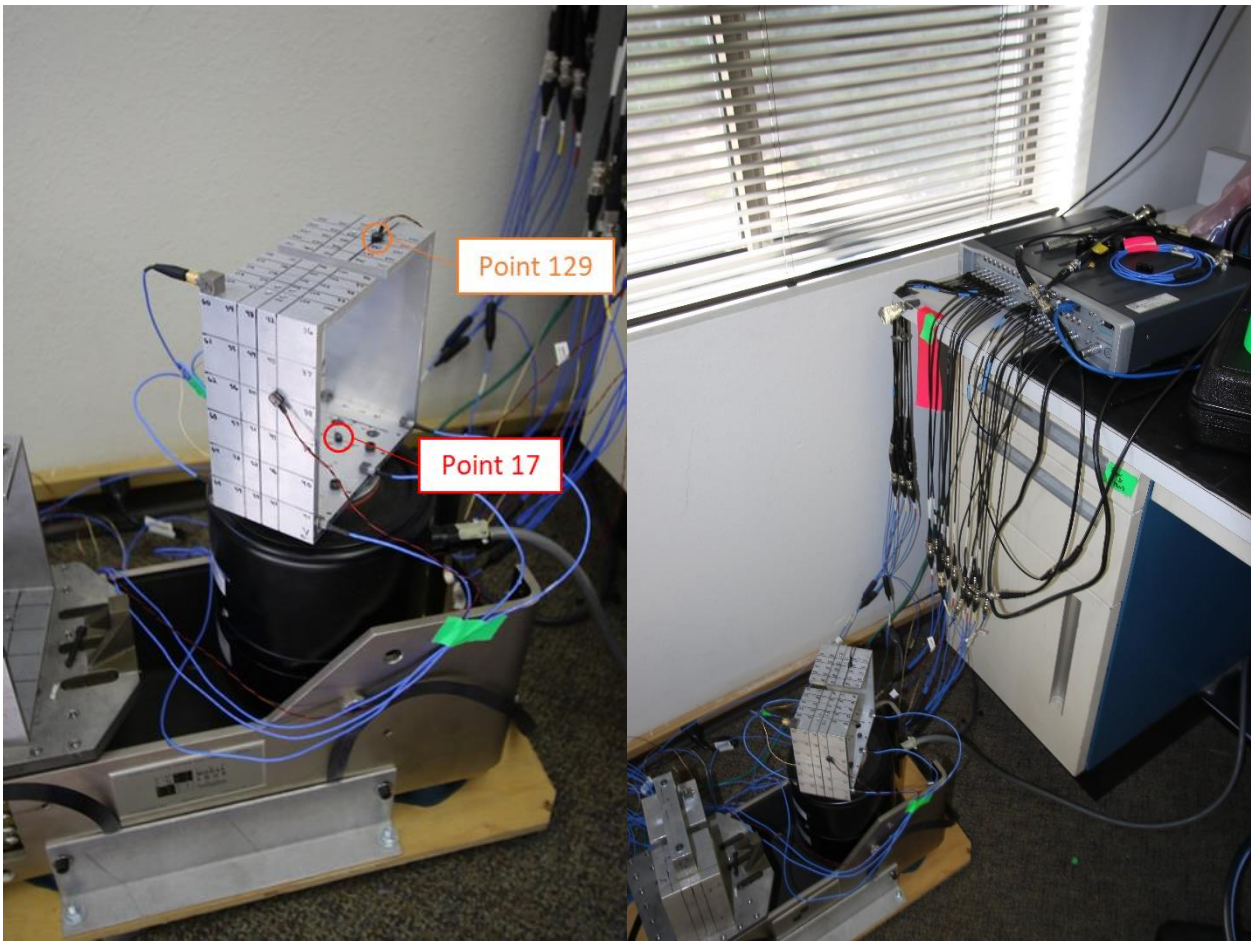


Figure 3.2.4 Setup of the substructure coupling validation test.

As with the test analysis performed for the shaker model validation, the impedance, acceleration over voltage, and acceleration over current FRFs were calculated from the time history data collected. Figures 3.2.5 through 3.2.7 show the FRFs calculated using the acceleration measurements at Point 17. This is a similar location to the table measurements made on the table, which was obscured by the test article. These FRFs clearly show the interaction of the BARC base's dynamics with the dynamics of the shaker. Not only are some of the modes from the BARC base seen, but the modes of the shaker have also been shifted by the change in mass of the system.

These results will be compared to the results of the substructure coupling analysis in the next section.

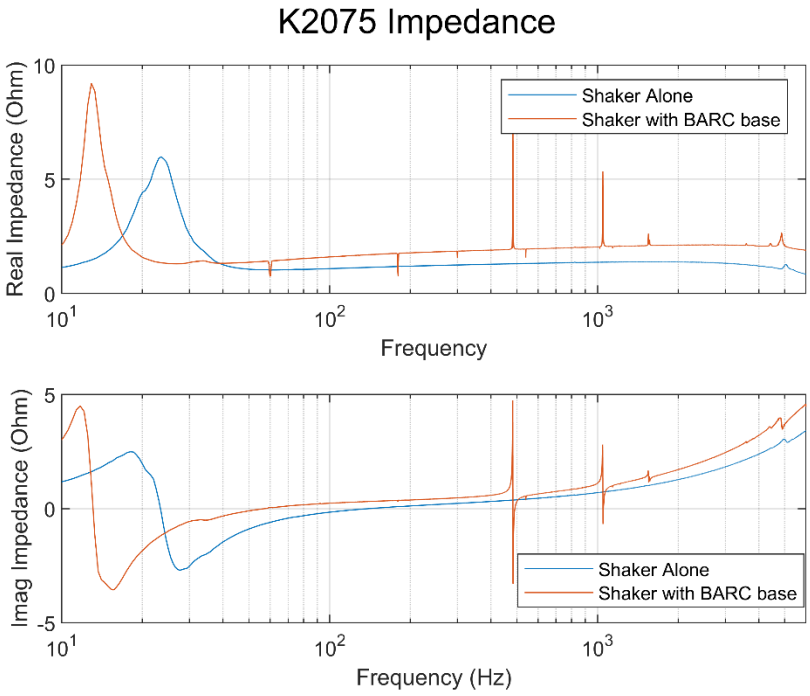


Figure 3.2.5 Comparison of the impedance with the shaker alone vs when coupled with the BARC base.

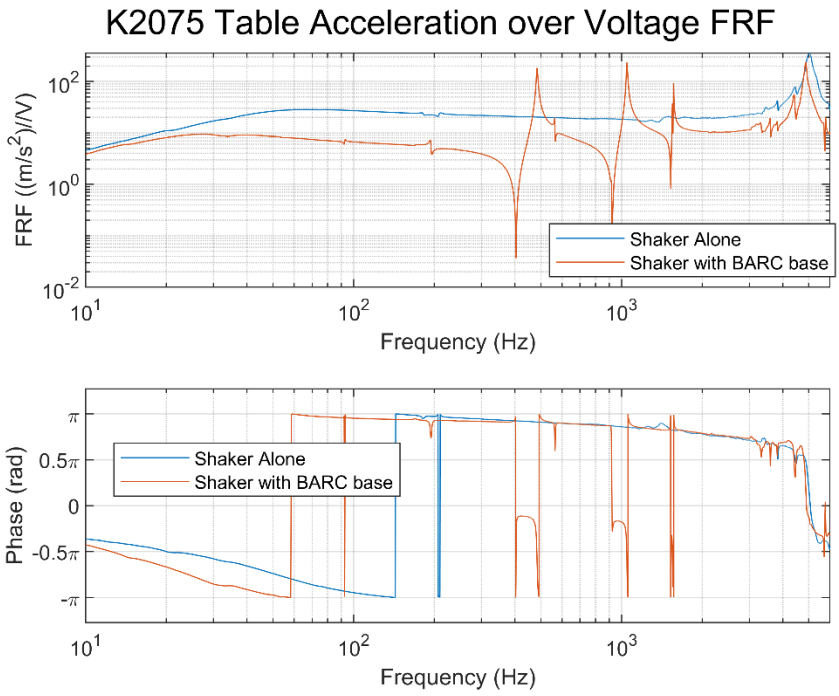


Figure 3.2.6 Comparison of the table acceleration over current FRF with the point 17 acceleration over current FRF.

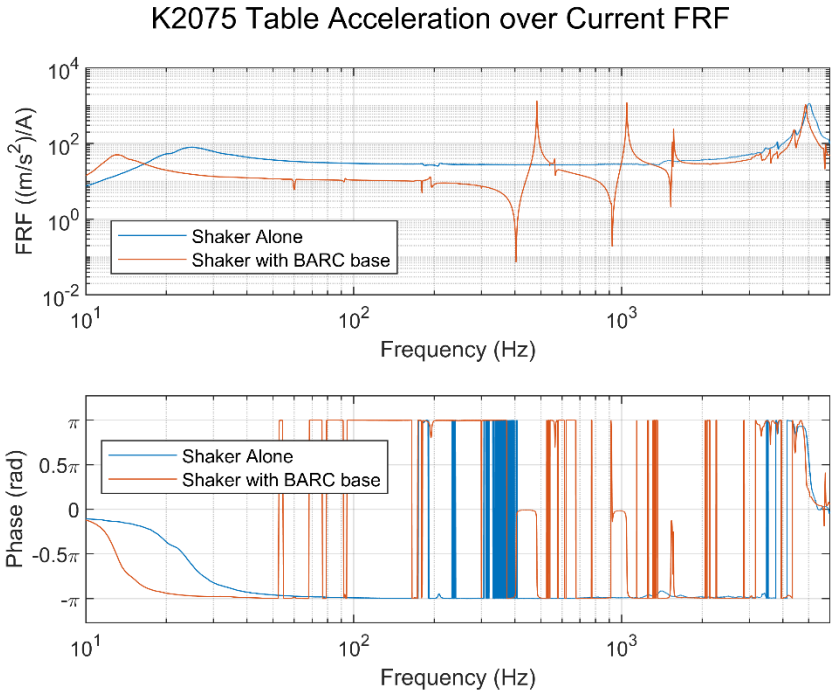


Figure 3.2.7 Comparison of the table acceleration over voltage FRF with the point 17 acceleration over current FRF.

*3.2.4 Substructuring Analysis Results*

The results of the coupling are shown in figures 3.2.8 through 3.2.12 and are compared to the validation testing results.

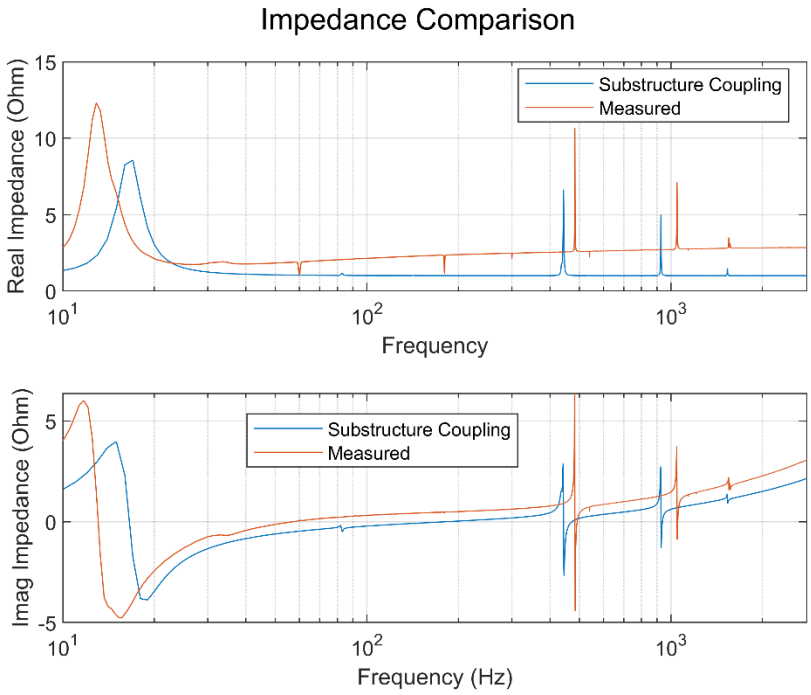


Figure 3.2.8 Impedance estimated from substructure coupling compared to measured impedance.

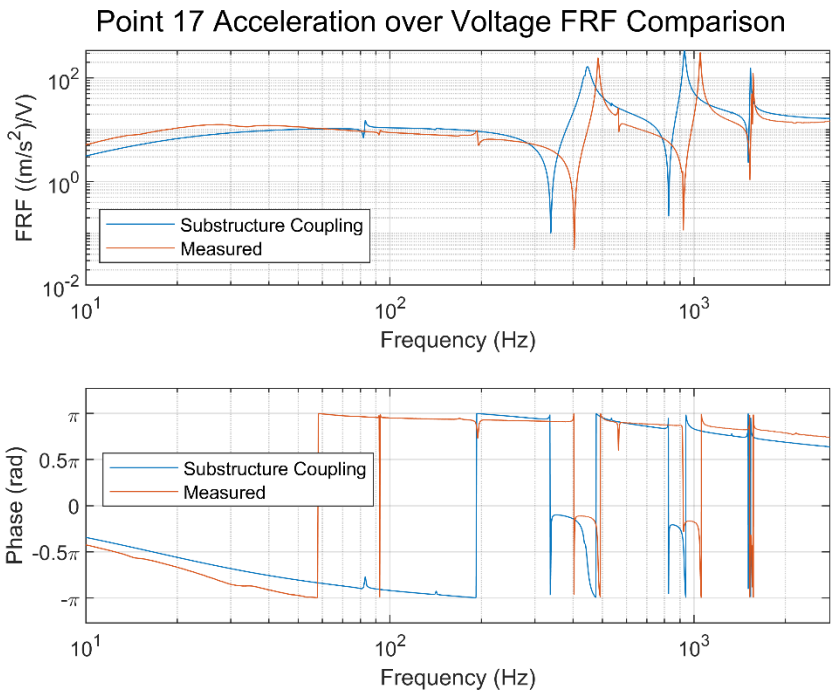


Figure 3.2.9 Acceleration over voltage FRF at Point 17 estimated from substructure coupling compared to measured acceleration over voltage FRF at Point 17.

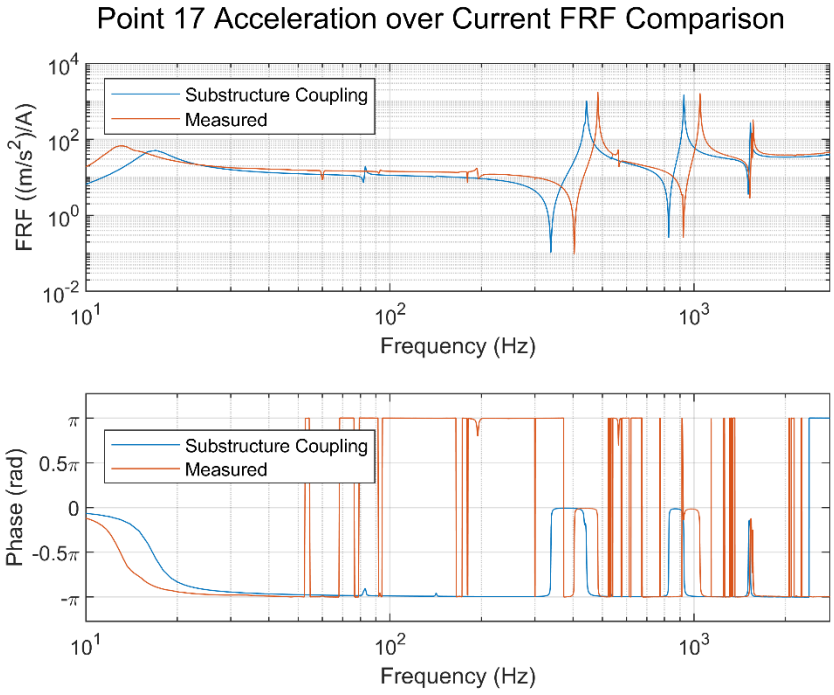


Figure 3.2.10 Acceleration over current FRF at Point 17 estimated from substructure coupling compared to measured acceleration over current FRF at Point 17.

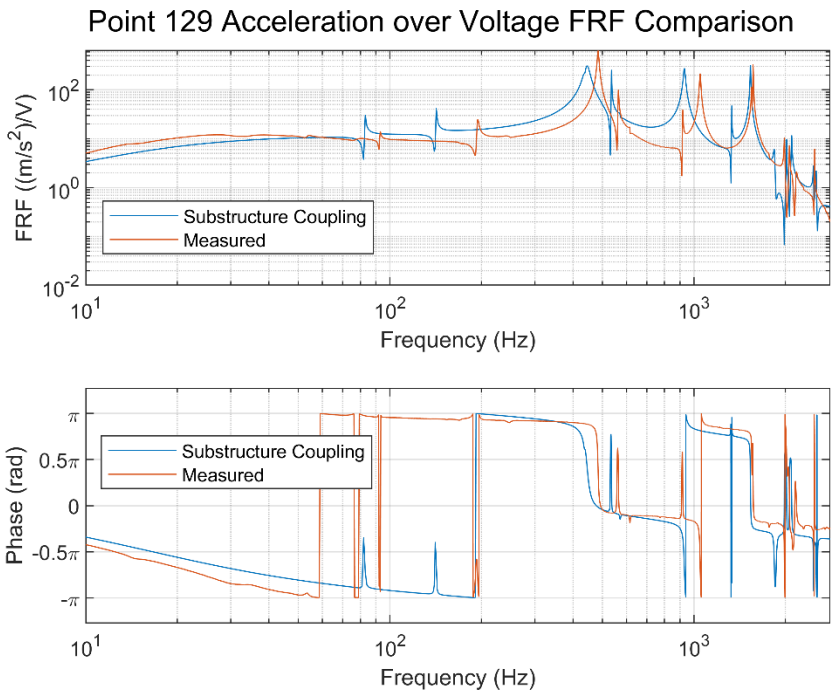


Figure 3.2.11 Acceleration over voltage FRF at Point 129 estimated from substructure coupling compared to measured acceleration over voltage FRF at Point 129.

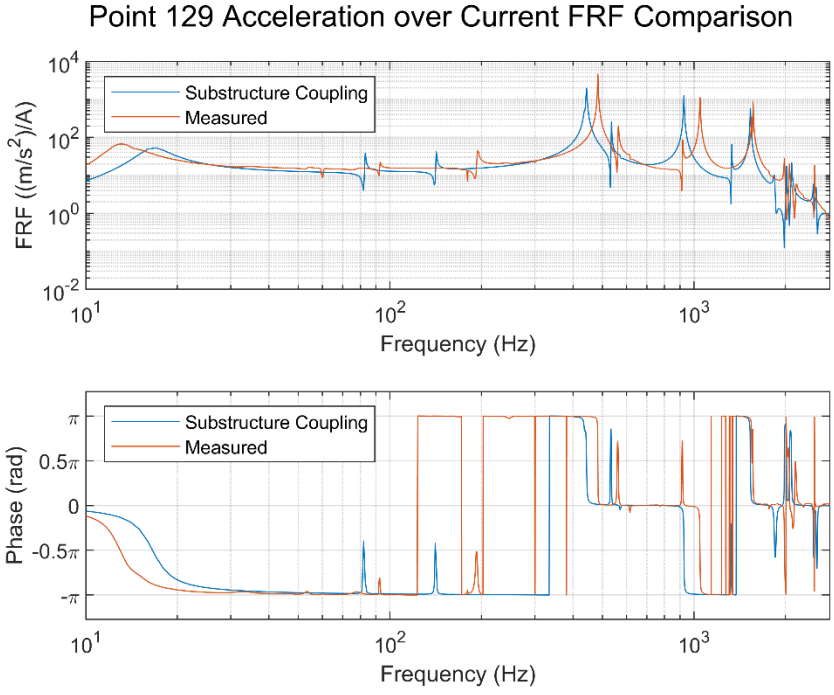


Figure 3.2.12 Acceleration over current FRF at Point 129 estimated from substructure coupling compared to measured acceleration over current FRF at Point 129.

The results of the substructuring analysis are not perfect but indicate, with improvement, the method could be used for predicting shaker capability. Points 17 and 129 are both uniaxial accelerometers measuring in the vertical direction. Point 17 was a coupling point between the modal model of the BARC base and shaker model, while point 129 is located on top of the BARC base. The frequency of the suspension mode, seen in the impedance and acceleration FRF, is overestimated. However, the remainder of the peaks seen are underestimated in frequency for all three FRFs. This underestimation indicates the substructure coupling is not as stiff as the true system. The substructure coupling is modeled through two rigid connections, while the physical structure is attached via four bolted connections. Further, the connections are only constrained in the vertical direction, while the bolted connections constrain all motion. The modeled motion is not representative of the number of constraints on the physical structure, resulting in a softer estimation of the coupled dynamics. However, the bolted connections are not truly rigid either, making an accurate representation of the physical coupling difficult. The errors seen could be improved by connecting the two substructures at the physical connection points, and by estimating the 6-DOF motion at those connection points. This could be achieved through the virtual point transformation or the transmission simulator.

### 3.3 Shaker Capability Estimation

The FRFs calculated in the previous section can be utilized to transform electrical inputs to the shaker into mechanical responses at the measured driving points, or vice versa. It is this relationship that will be used to perform shaker capability estimation. The inverses of the FRFs can be used as filters on acceleration test specifications to determine the electrical inputs required to meet those specifications. Alternatively, random acceleration signals satisfying the test

specifications can be generated and transformed by the FRFs to estimate the expected electrical input signals.

*3.3.1 Transforming the Test Specification*

The test specification used in the substructuring analysis validation test, a 1.5 gRMS flat-band PSD controlled at Points 17 and 19, is considered. For this example, the specification is trimmed to the maximum range of the modal parameter estimation, 10 Hz to 2800 Hz. The trimming of the spectrum results in approximately a 1 gRMS specification. This is representative of a typical diagnostic random test profile used in vibration testing. The goal is to determine the electrical requirements to achieve the acceleration profile, so the inverse of the acceleration FRFs estimated from the substructuring analysis are taken, shown in Figure 3.3.1. The inverse FRF calculated from the test data is also shown and will continue to be used to illustrate the success of the capability estimation method when a well-estimated FRF is used. Because this FRF was calculated based on the test data itself, it represents the ideal case.

The test specification is given as a PSD, so the square of the norm of the FRF must be used to filter the specification back to the electrical inputs required to achieve it,

$$\mathbf{R}_{\mathrm{V}} = \left|\mathbf{H}_{\mathrm{V/a}}\right|^{\mathbf{2}}\mathbf{R}_{\mathrm{a}}, \tag{3.8}$$

where $\mathbf{R}_{\mathrm{v}}$ is the estimated voltage input PSD, $\mathbf{H}_{\mathrm{V/a}}$ is the voltage over acceleration FRF from Figure 3.3.1a, and $\mathbf{R}_{\mathrm{a}}$ is the acceleration test specification PSD. The test specification and FRF are multiplied on a frequency-line bases in the frequency domain to filter the specification by the norm-square FRF. In order to perform this filtering, the FRF must first be interpolated to the same frequency lines as the test specification. A linear interpolation was used.

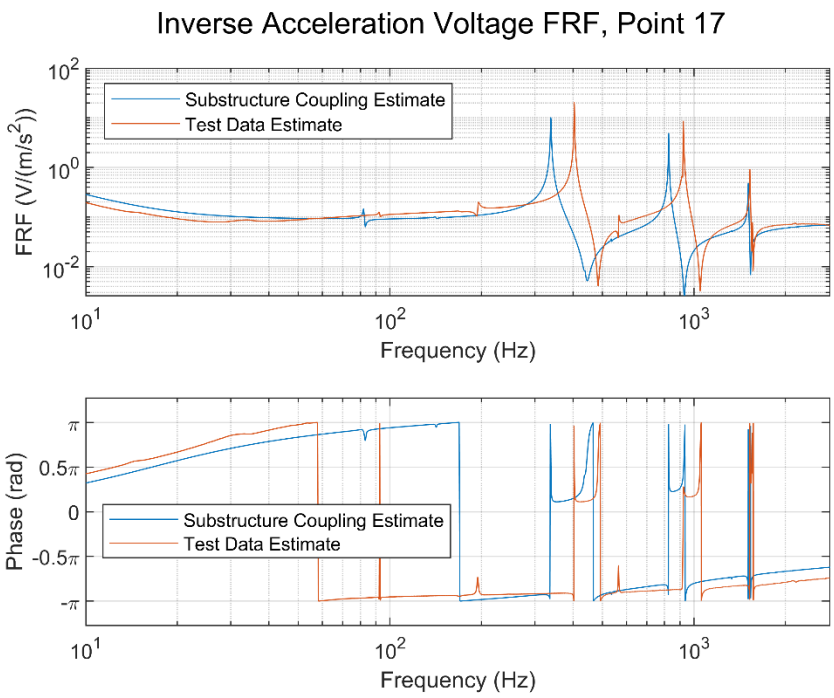


(a)

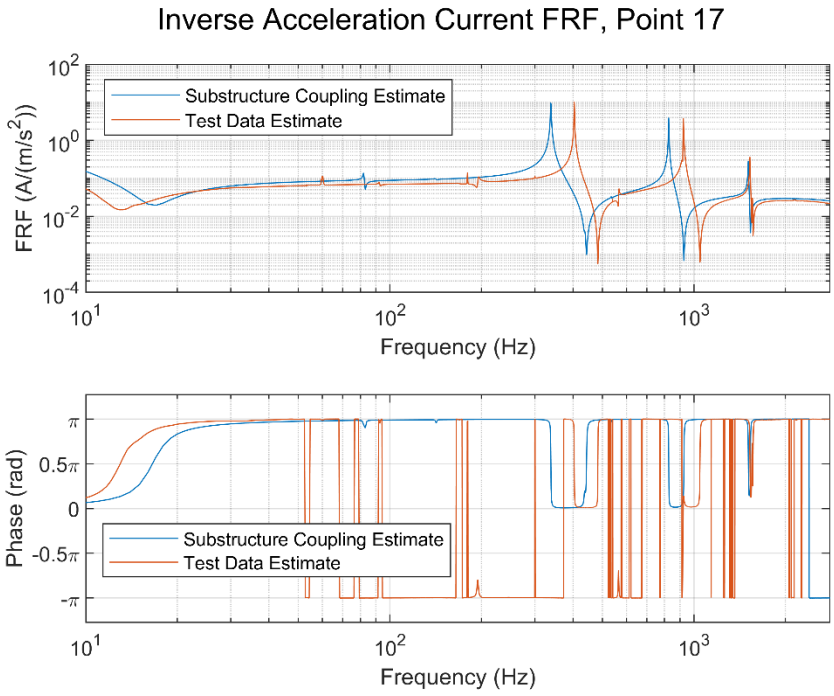


(b)

Figure 3.3.1 Inverse FRFs to use for transforming test specification to electrical requirements.

The results of the transformation are shown in Figure 3.3.2. Because the specification used for this calculation was actually tested, it may be directly compared to the actual voltage input for the test, filtered to the same 10 Hz to 2800 Hz limits.

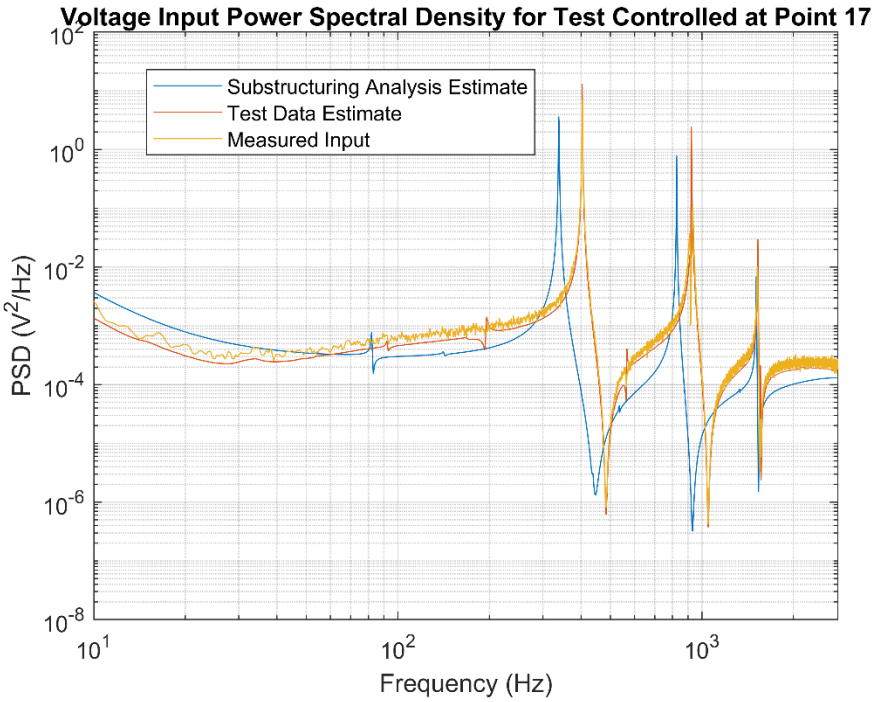


Figure 3.3.2 Estimate of the voltage input spectrum required for a random vibration test compared to the measured voltage input of a test using the same specification.

The same analysis can be performed using the acceleration-current FRF, or by using the impedance to transform the voltage input estimate into an estimate of the current input. The results of using the acceleration-current FRF following the same process are shown in Figure 3.3.3.

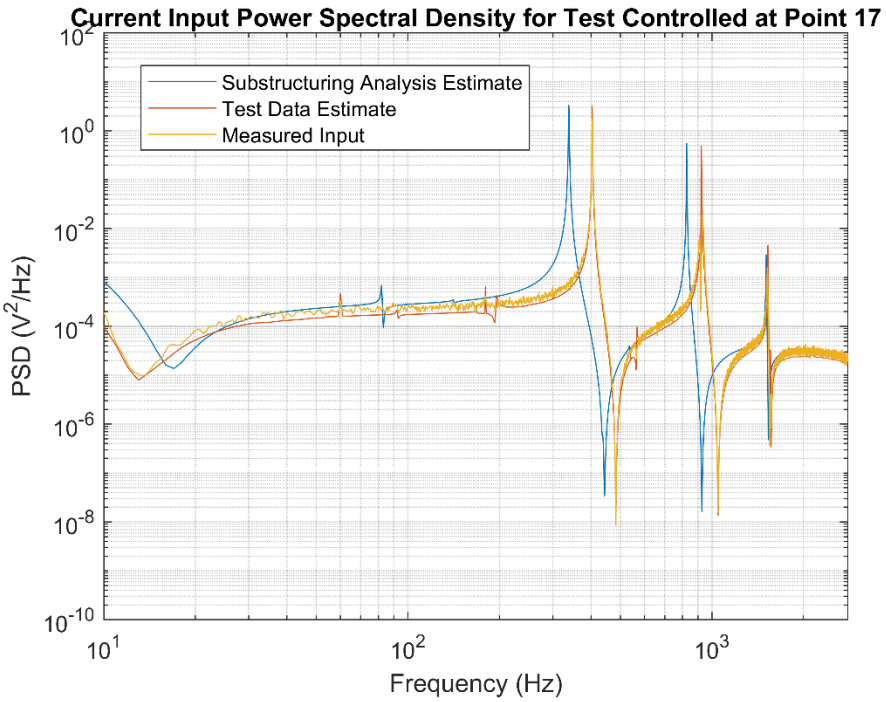


Figure 3.3.3 Estimate of the current input spectrum required for a random vibration test compared to the measured current input of a test using the same specification.

The errors in the FRF from the substructuring analysis propagate through this analysis. The underestimation of the natural frequencies in the FRFs result in an underestimation of the peaks seen in the input power spectra. However, the FRF calculated from the test data, as expected, makes a very accurate estimate of the spectra.

These PSDs can be integrated to find the expected RMS of the electrical input signals and compared to the specification sheet for the amplifier being used. Estimates of the peak value may also be calculated based on simple statistics of signals. The RMS of a zero-mean, gaussian distributed signal is equivalent to the standard deviation, so the RMS estimate from the PSDs calculated can be used to determine the statistical distributions of the signals. Many control softwares offer "sigma limiting" capabilities, where the controller attempts to prevent any instantaneous accelerations beyond a user-specified standard deviation. The validation test

conducted utilized a sigma limiting level of five standard deviations, so one may assume a peak value of 5-sigma. Assuming the entire transformation is linear, the maximum allowable value for the electrical inputs would also be at a 5-sigma level, as gaussian random processes remain gaussian after a linear transformation.

Table 3.3 shows the estimated RMS and peak values of the electrical inputs from the substructuring analysis, the values estimated from the test data FRF, and the actual values from the measured signals.

Table 3.3.1 RMS and Peak Value Estimates Comparison for Test Specification Transformation

| | **Substructuring Analysis FRF Estimate** | | **Test Data FRF Estimate** | | **Measured** | |
|---|---|---|---|---|---|---|
| **Type** | RMS | Peak | RMS | Peak | RMS | Peak |
| **Voltage (V)** | 3.431 | 17.15 | 5.807 | 29.03 | 5.613 | 23.39 |
| **Error (%)** | -38.87 | -26.65 | 3.452 | 24.13 | - | - |
| **Current (A)** | 3.220 | 16.10 | 2.819 | 14.09 | 2.786 | 10.82 |
| **Error (%)** | 15.56 | 48.78 | 1.172 | 30.25 | - | - |

The RMS and peak values from the substructuring analysis severely underestimate the voltage input required, while slightly overestimating the current input required. The FRF developed from the test data makes an accurate estimate of the RMS but overestimates the peak value. The sigma limiting of the software attempts to set a maximum threshold of the “peak value” estimated here, therefore it is somewhat unsurprising that the 5-sigma estimate definition of “peak value” is too high, as it represents more of an upper bound. Both measured maximum values occur at approximately four standard deviations, rather than five. In addition, any overestimation of the

RMS results in an overestimation of the peak value. The limitations specified for the amplifier used, a 2050E05 Linear Amplifier from the modal shop, are 25 VRMS and 20 ARMS. The substructuring analysis correctly labels this test as feasible with the given equipment but may incorrectly predict a higher level as feasible because of the underconservative estimate of input voltage.

### *3.3.2 Transforming the Time Domain Signal*

Rather than transforming the test specification itself, a realization of a random time signal satisfying the test specification may be generated and similarly filtered by the inverted frequency response function. Figure 3.3.4a shows a realization of a random time signal satisfying the 1 gRMS, 10 Hz to 2800 Hz specification compared to the measured acceleration time data from the validation test, again filtered to a range of 10 Hz to 2800 Hz for consistency. Figure 3.3.4b shows an overlayed histogram of the two signals, indicating they are from very similar distributions.

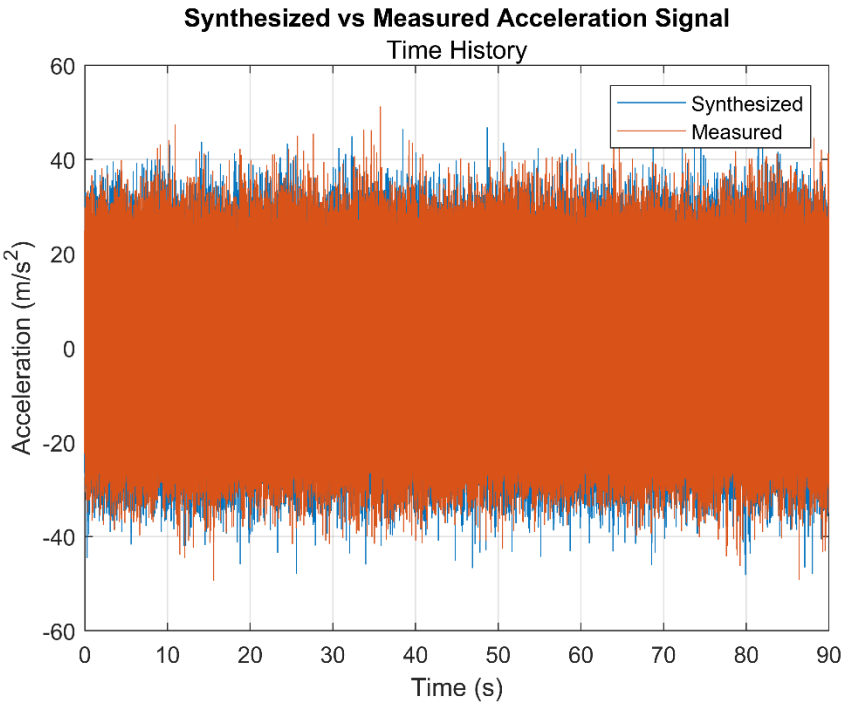


(a)

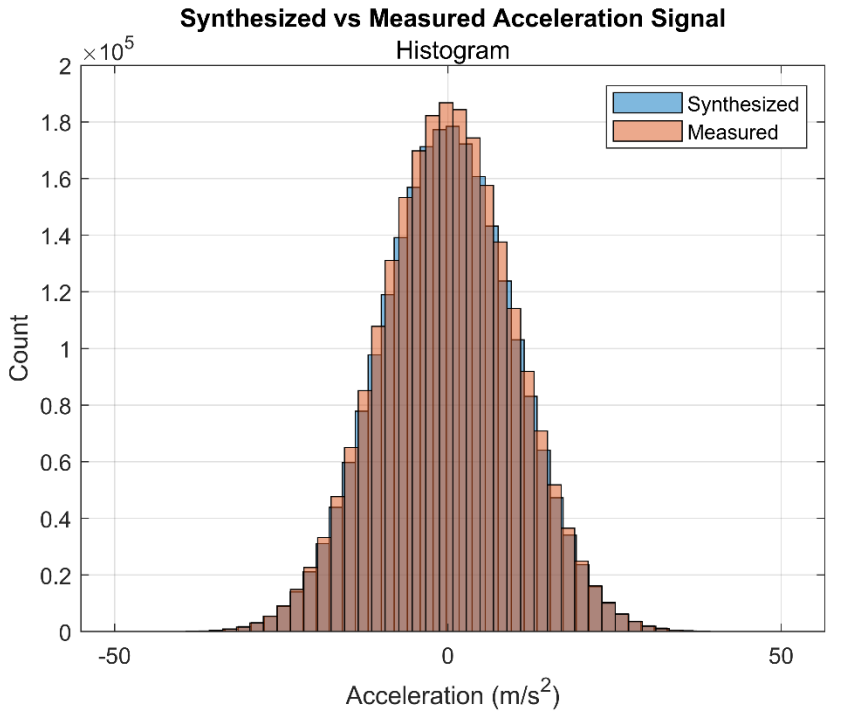


(b)

Figure 3.3.4 Comparison of a synthesized time signal satisfying the test specification vs the measured acceleration achieved from that specification.

This time signal can then be filtered by the FRFs to estimate the input time histories for the current and voltage that must be supplied by the amplifier. This is best achieved in the frequency domain. First the discrete Fourier transform of the time signal is taken. Then it is multiplied on a frequency-line basis with the FRF,

$$\mathbf{S}_V = \mathbf{H}_{V/a}\,\mathbf{S}_a. \tag{3.9}$$

$\mathbf{S}_V$ is the DFT of the voltage input signal, $\mathbf{H}_{V/a}$ is the voltage-amplitude FRF, and $\mathbf{S}_a$ is the DFT of the acceleration output signal. Finally, the inverse discrete Fourier transform of the filtered signal is calculated to estimate the input time history. Figures 3.3.5 and 3.3.6 show the time histories and histograms of the estimated input signals from the two FRFs compared to the measured input signals. Table 3.4 contains the estimated RMS and peak values from the estimated input signals.

Table 3.3.2 RMS and Peak Value Estimates Comparison for Time Domain Signal Transformation

| | **Substructuring Analysis FRF Estimate** | | **Test Data FRF Estimate** | | **Measured** | |
|---|---|---|---|---|---|---|
| **Type** | RMS | Peak | RMS | Peak | RMS | Peak |
| **Voltage (V)** | 3.178 | 15.89 | 5.725 | 28.62 | 5.613 | 23.39 |
| **Error (%)** | -43.38 | -32.06 | 1.992 | 22.38 | - | - |
| **Current (A)** | 2.972 | 14.86 | 2.776 | 13.88 | 2.786 | 10.82 |
| **Error (%)** | 6.88 | 37.35 | -0.3633 | 28.27 | - | - |

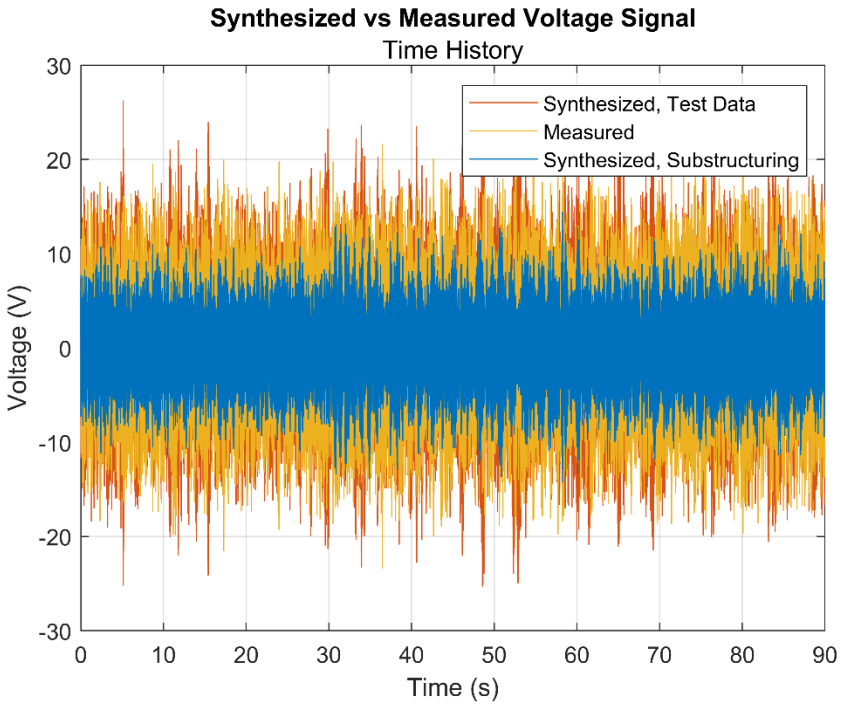


(a)

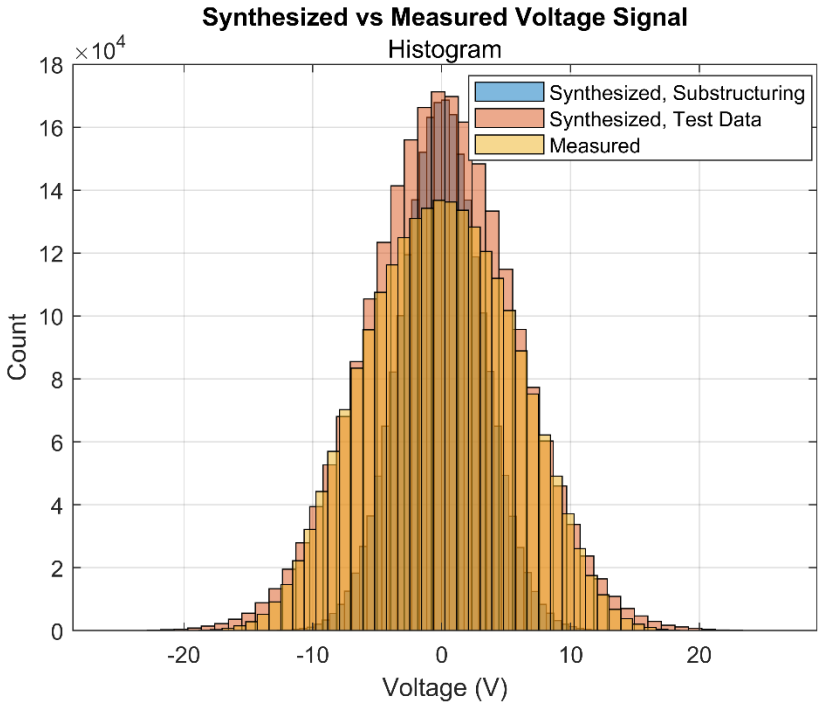


(b)

Figure 3.3.5 Comparison of estimates for the input voltage signal to the measured input voltage signal.

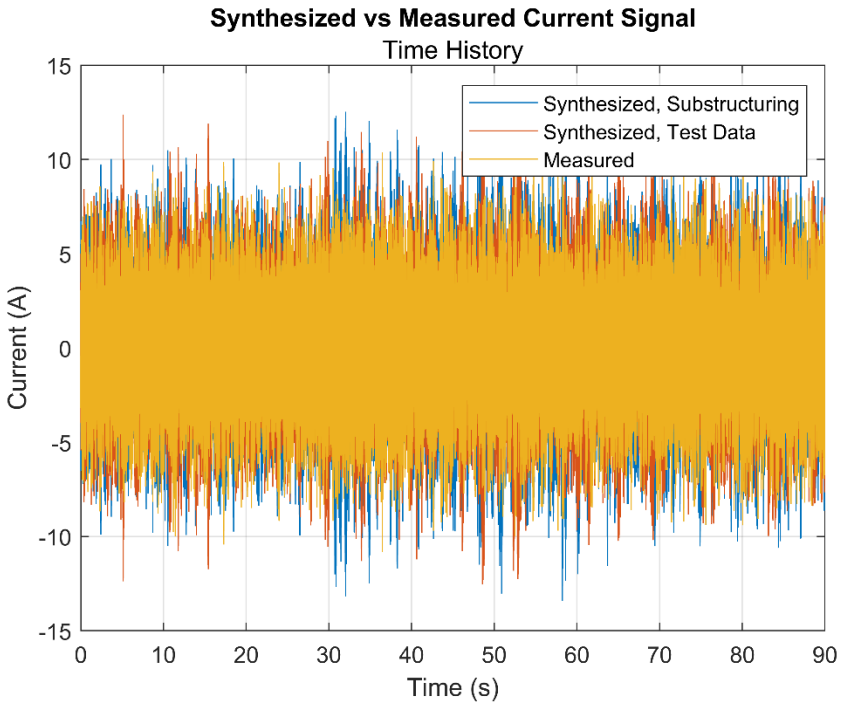


(a)

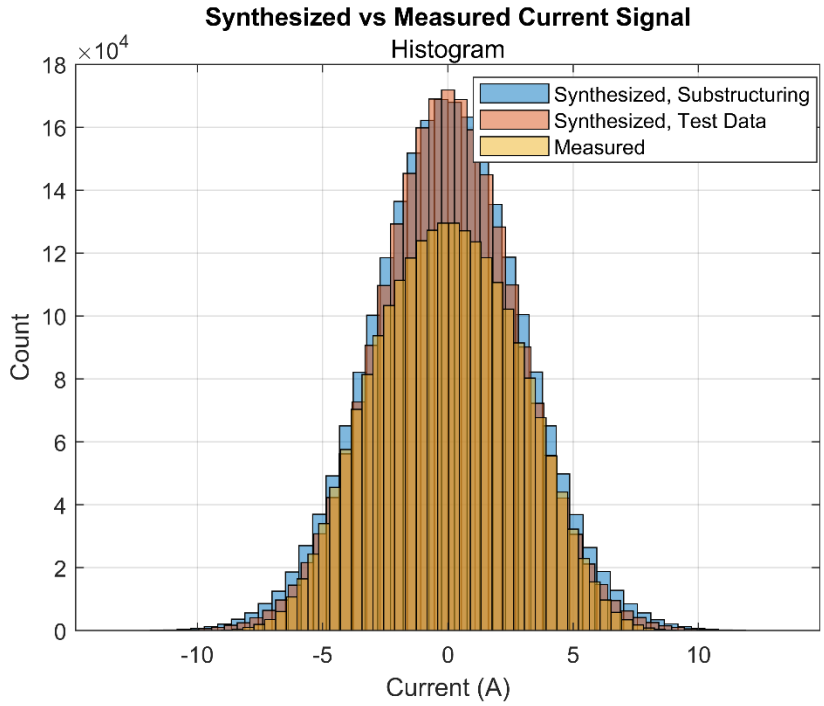


(b)

Figure 3.3.6 Comparison of estimates for the input current signal to the measured input current signal.

Again, the RMS and peak values of the input voltage signal are underestimated, while the current RMS and peak values are slightly overestimated. However, the transformation of a representative time domain signal does offer slightly better estimates of the RMS and peak value of the signal in the ideal case. The time domain signals appear similar but are difficult to interpret visually. The histograms provide a clearer understanding of the time data and show that while the test data FRF performed better at estimating the input signals using this method, the distribution of the input signals is not completely captured. The distribution of the measured signal has a lower peak, despite the same tail distribution. A fit of a normal probability density function (PDF) to the measured data, seen in figure 3.6.7, shows it is not quite normally distributed, indicating the actual relationship between the electrical inputs and acceleration response is not linear, which is an assumption that was made for this analysis.

This method of transforming a time domain signal using the measured FRF is the same method utilized by many commercial control software packages in order to estimate the feasibility of a test. It can also be used to estimate input signals for mechanical shock testing when a time waveform is specified. However, it is more difficult to execute, as it requires the generation of random signals to satisfy the test specification, as well as transforming those signals using the FRFs.

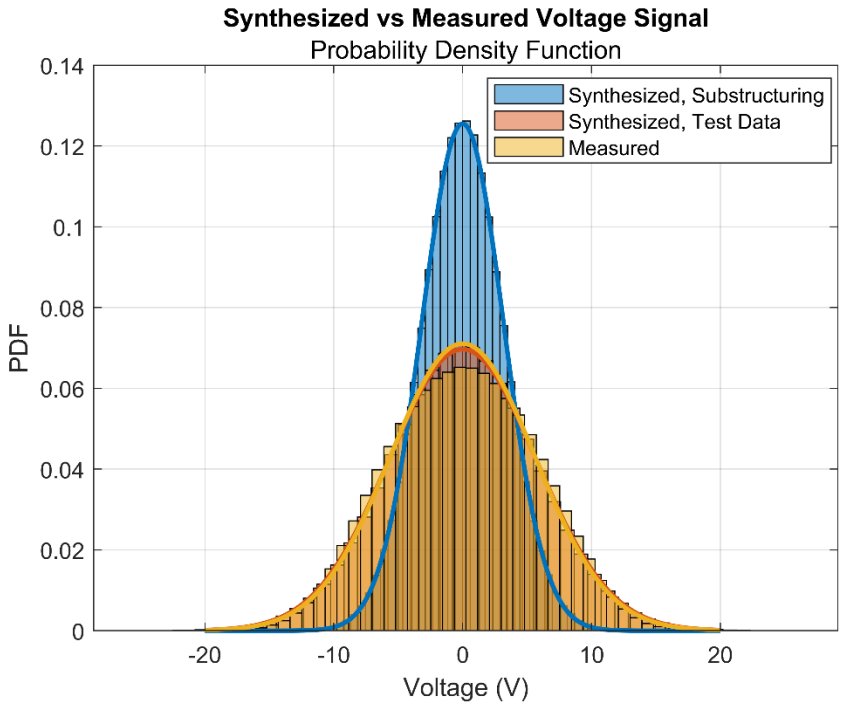


(a)

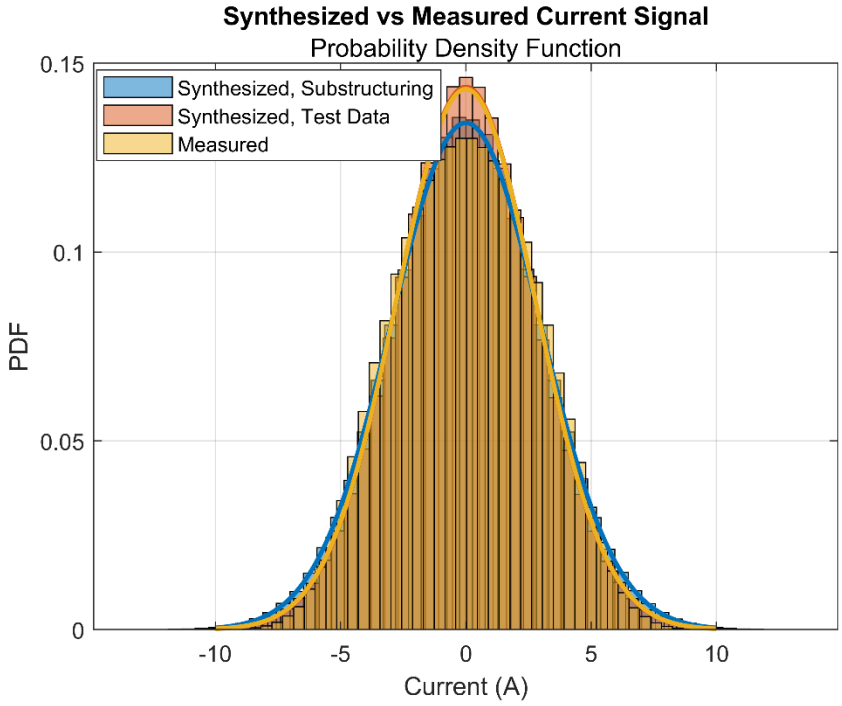


(b)

Figure 3.3.7 Synthesized and measured (a) voltage and (b) current data histograms compared to their normal distribution fits.

# 4.0 DISCUSSION AND CONCLUSIONS

## 4.1 Discussion

### *4.1.1 Shaker Modeling*

The results of the shaker model adequately matched the dynamics of the 75 lbf dual-purpose shaker used for this work. However, the model could both be simplified and at the same time made more complex. The inclusion of the body DOF does not appear to be necessary in the frequency range that was tested. The isolation mode most associated with this DOF was not observed in the test data collected and did not improve the performance of the model. The model assumed the mass of the body of the shaker at just 15.55 kg, which is the mass provided by the manufacturer in the specification sheet. This mass is just for the black body housing seen in Figure 3.1.1, but the shaker is nearly rigidly assembled into a fixture containing a slip-table. The combination of the fixture, slip table, and body together constitute a much larger mass than 15.55 kg, pushing the actual expected frequency much lower than was modeled. Second, the shaker was placed on a layer of foam in an attempt to isolate it from the floor and reduce disturbances to neighboring work in the testing area. The foam used is program material for drop tower testing and is very dissipative, significantly damping energy that would be seen in the isolation mode. Removing the mode would both simplify the model and reduce the solution space for the optimization algorithm used when updating the model.

In addition to removing the body degree-of-freedom from the model, further improvements should be made to the optimization used for model updating. More work must be done to identify confounding parameters, such as the coil stiffness and the coupling coefficient, and further constraints implemented to prevent these factors from compensating for one another. Six

parameters remains a large solution space, so combining parameters that are not independent would further reduce the solution space and likely improve updating results results.

The model may benefit from *increasing* complexity by adding in other DOFs to capture more detailed motion of the shaker, as was done by Hoffait et al [15]. Including a rotational DOF or a second translational DOF could begin to capture out-of-axis motion of the shaker and possibly improve the results of the substructure coupling analysis. While the armature moves predominantly in the vertical direction, there is certainly some motion in other directions that influences the results of a test.

### *4.1.2 Experimental Dynamic Substructuring Implementation*

The results of the experimental dynamic substructuring implementation were not as successful as the shaker modeling. While the BARC base was well-characterized in the range tested it wasn't possible to get a fit of the full range of interest, which would include the shaker's coil resonance at about 5300 Hz. The coil resonance and beyond is the area of most interest because the resonance creates control difficulties, and the more complicated dynamics beyond it present more limitations than the flat region below it. Substructuring also requires a strong characterization of the rigid body modes, as they describe most of the motion occurring at interfaces. Exciting such a wide range of dynamics is difficult to do with impact testing, but shaker modal testing is not feasible with the number of driving points needed.

Beyond modal testing, experimental FBS is well-documented as difficult to implement. The LaGrange-Multiplier Frequency-Based-Substructuring method used is the most basic approach to FBS and has a number of drawbacks discussed in section 2.7. The issue of measurement noise was successfully dealt with by utilizing synthesized frequency response functions from the modal parameter estimation of the data, but other issues remained. No rotational

degrees of freedom were estimated, and the two connection points used, 17 and 19, while in the vicinity of the interface, were not collocated with the physical connections. As a result, the torsional modes, not clearly seen in Point 17 but clearly seen in Point 129, were poorly estimated. At point 129, the modes seen near 1000 Hz are estimated in the wrong order in the substructure coupling, with a bending mode 900 Hz, where torsion mode was measured. The following mode estimated was a torsion mode near 1500 Hz, when a bending mode was measured at lower frequency. Overall, the substructure coupling underestimated the stiffness of the coupling between the shaker and the BARC base, resulting in natural frequency estimates that were too low. It is likely this is because of the coupling approach chosen. Four physical connections coupled the two substructures together, but only two were used analytically. The analytical coupling also only used the vertical DOFs. The shaker model only contained vertical motion at the table, but all of the 6-DOF motion at each physical connection is constrained by the bolts, making the connection stiffer than was modeled.

Some approaches that may alleviate these issues would be the use of the virtual point transformation or the transmission simulator. Both methods present a different set of challenges from those of the LM-FBS method used. The virtual point method suggests using three triaxial accelerometers around each virtual point to estimate the 6-DOF motion at that point. The 9-DOF measurements are projected to the 6-DOF space via interface displacement modes that are determined based on the rigid body modes. This projection then estimates the 6-DOF motion in a least squares sense, averaging out measurement errors. Several issues with the test article chosen occurred when attempting this method. First, the rigid body modes need to be well-characterized, which was not achieved in the modal test conducted. Second, the plate-like structure on the bottom of the article makes it difficult to achieve driving points in all three translational directions. At the

corners of the plate, all three translations may be measured, but at the edge, only two, and in the middle, just one. Tapping blocks may be used to excite these other translations, but at the risk of mass-loading the test article because of its small size. So, only six DOFs are measurable. While theoretically enough to estimate the 6-DOF motion at each of the necessary virtual points, the least-squares estimation of the motion is lost, leaving it more susceptible to measurement errors and poor matrix conditioning. Lastly, a balance must be made between the distance from the virtual point and the measurement locations. Sensors further away offer better estimations of the dynamics at the virtual point, but the method assumes rigid translation between the sensors and the virtual point. This assumption is valid up to the frequency where elastic motion between the sensors and virtual point begins to occur, which decreases with increases in distance. The spacing of the sensors on the plate would likely not allow an adequate dynamic range to be characterized before the assumption is no longer valid.

A transmission simulator (TS) method may also improve the results of the substructuring. This method utilizes a fabricated interface that is analytically modeled and physically tested. The model is then coupled to the modeled substructure and the physical object to the experimentally characterized substructure. The two substructures are then joined by constraining the motion of the transmission simulator in the model and from the experiment to be the same. This then estimates the 6-DOF motion using the model and estimates the physical motion at the interface from the test. This is an attractive method of substructuring for this particular problem because the interfaces of the shaker tables and slip tables will not change, so a single TS may be fabricated for any and all shakers of interest and reused for multiple tests. The difficulties with this method, beyond having to fabricate the TS for each shaker, are with modeling and the properties of the interface. The model used for this work contained just one vertically translating DOF for the table,

which may oversimplify the motion on the model side of the interface and no longer help the method. A more complex model could be developed to alleviate this issue. The TS method is ideally suited for continuous interfaces between substructures, while the virtual point method is ideal for discrete connections. However, the inserts of the armature table are essentially raised washers embedded in the table, creating an interface somewhere in-between a series of discrete connection points and a continuous surface. Creating a TS to represent this interface accurately could be difficult.

### *4.1.3 Shaker Capability Estimation*

The errors in the substructuring results propagate through the method of estimating shaker capability, resulting in an underestimate of the voltage and an overestimate of the current. These two inputs are related by the impedance of the system, so a better estimate of the impedance is needed. However, the estimates using the test data were very accurate, especially when transforming representative time-domain signals. This shows the estimates are very dependent on the FRF used, so it is imperative to accurately characterize the system. The method of transforming the test specification showed slightly more error than transforming time-domain signals, likely because the transformation uses the norm-squared FRF, which accentuates any errors in the function. However, it is a simpler technique, because time-domain signals representative of that test specification do not need to be generated. Transforming the time-domain signals offered slightly better results for estimating shaker capability, and is also applicable to mechanical shock testing, but requires the generation of time signals that satisfy the specification.

A number of assumptions were made in these estimations that may not always be true depending on the test control software used and the specific test setup. First, assumptions of linearity were made throughout this entire work, but many complex test articles show strong

nonlinearity. Normal PDF fits of the measured data indicated the simple system tested here was not quite linear. Second, assumptions were made that the desired acceleration output is normally distributed, which may or may not be true depending on how the signal is generated. If the signal is not gaussian, estimates of the peak value are more difficult to achieve and the RMS is not as descriptive of the signal. Lastly, not all control software may implement sigma limiting, or allow the user to choose the level of sigma limiting. This again makes it difficult to estimate what the peak value seen may be.

### 4.2 Conclusions and Recommendations

This work explored concepts of shaker modeling, modal testing, and experimental dynamic substructuring and applied them to develop a process for estimating shaker capability with more detail. Portions of this process were achieved with success, such as the shaker modeling, while others need improvement, such as the experimental dynamic substructuring. The results show that the process is possible but highly dependent on the ability to accurately characterize the frequency response functions relating the acceleration response at the control location to the electrical inputs to the shaker. When these FRFs are accurately characterized, the RMS and peak value of the inputs required can be estimated within 3.5% and 30% error respectively. However, when the estimation of the FRFs is not accurate, the method sees much larger error. The use of unmodified LaGrange-Multiplier Frequency-Based-Substructuring is not recommended, as it is difficult to accurately couple the shaker model to the DUT, resulting in a poor estimation of the FRFs. Other methods, such as the virtual point transformation or transmission simulator should be explored to improve these estimations and achieve better results for capability estimation. While this work focused on random vibration testing, these same methods may be applied to mechanical shock testing using

electrodynamic shakers. Further work should be conducted to explore applying these methods to shaker shock and the fidelity with which shock capability can be estimated.

This thesis, in portion, is a reprint of material as it appears in the Conference Proceedings of the 41st International Modal Analysis conference, 2023. Peter H. Fickenwirth, Michael D. Todd, John F. Schultze, Dustin Y. Harvey, Springer, 2023. The thesis author was the primary investigator and author of this paper.

## 5.0 REFERENCES


[1] M. S. Allen, D. Rixen, M. Van Der Seijs, P. Tiso, T. Abrahamsson, and R. L. Mayes, *Substructuring in Engineering Dynamics*. Vol. 594. CISM International Centre for Mechanical Sciences. Cham: Springer International Publishing AG, 2019.

[2] G. Strang, *Introduction to Linear Algebra*. 3rd Ed., Rev. International ed. Wellesley, MA: Wellesley-Cambridge Press, 2005.

[3] P. Avitabile, *Modal Testing*. 1st ed. Hoboken, NJ: Wiley, 2017.

[4] V. Ingle, S. Kogon, D. Manolakis, *Statistical and Adaptive Signal Processing*, Artech, 2005.

[5] K.G. McConnell, *Vibration Testing: Theory and Practice*. New York: John Wiley, 1995.

[6] C.G. Fox, "An Inverse Fourier Transform Algorithm for Generating Random Signals of a Specified Spectral Form." *Computers & Geosciences* vol. 13, no. 4, pp. 369-74, 1987.

[7] S. S. Rao, *Engineering Optimization*. 5th ed. Newark, Wiley, 2020.

[8] G. F. Lang, "Electrodynamic Shaker Fundamentals," *Sound and Vibration*, 1997 Apr.

[9] G. F. Lang and D. Snyder, "Understanding the Physics of Electrodynamic Shaker Performance," *Sound and Vibration*, vol. 35, no. 10, pp. 24-33, 2001 Oct.

[10] J. Martino and K. Harri, "Virtual shaker modeling and simulation, parameters estimation of a high damped electrodynamic shaker," *International Journal of Mechanical Sciences*, vol. 151, pp. 375-384, 2019.

[11] R. Schultz, "Calibration of Shaker Electro-mechanical Models," *Proceedings of the 38th IMAC*, 2020.

[12] R. L. Mayes, L. Ankers, P. M. Daborn, T. Moulder, and P. Ind, "Optimization of shaker locations for multiple shaker environmental testing," in *Proceedings of IMAC XXXVII, the 37th International Modal Analysis Conference*, 2019.

[13] S. Ricci, B. Peeters, R. Fetter, D. Boland, J. Debille, "Virtual Shaker Testing for Predicting and Improving Vibration Test Performance," *Proceedings of the IMAC-XXVII*, 2009.

[14] S. Manzato, F. Bucciarelli, M. Arras, G. Coppotelli, B. Peeters, and A. Carrella, "Validation of a Virtual Shaker Testing approach for improving environmental testing performance," *Proceedings of ISMA 2014 - International Conference on Noise and Vibration Engineerin*g, 2014.

[15] S. Hoffait, F. Marin, D. Simon, B. Peeters, and J. C. Golinval, "Measured-based shaker model to virtually simulate vibration sine test," *Case Studies in Mechanical Systems and Signal Processing*, vol. 4, pp. 1-7, 2016.

[16] P. S. Varoto, L. P. R. De Oliveira, “Interaction between a vibration exciter and the structure under test” *Sound and Vibration,* 2002.

[17] N. Tiwari, A. Puri, and A. Saraswat, "Lumped parameter modelling and methodology for extraction of model parameters for an electrodynamic shaker," *Journal of Low Frequency Noise, Vibration and Active Control*, vol. 36, no. 2, pp. 99-115, 2017.

[18] D. O. Smallwood, "Characterizing Electrodynamic Shakers," *Annual technical meeting and exposition of the Institute of Environmental Sciences*, 1997.

[19] D. de Klerk, D. Rixen, S. N. Voormeeren, “General Framework for Dynamic Substructuring: History, Review, and Classification of Techniques,” *AIAA Journal,* vol. 6, no. 5, pp 1169-1181, 2008.

[20] S. Rubin, “Mechanical Immitance- and Transmission-Matrix Concepts,” *Journal of the Acoustical Society of America,* vol. 41, no. 5, pp 1171-1179, 1967.

[21] J. R. Crowley, A. L. Klosterman, G. T. Rocklin, H. Vold, “Direct Structural Modification Using Frequency Response Functions,” *Proceedings of the II International Modal Analysis Conference (IMAC),* 1984, pp 58-65.

[22] B. Jetmundsen, *On Frequency Domain Methodologies for Structural Modification and Subsystem Synthesis*, Ph.D. thesis, Rensselaer Polytechnic Institute, Troy, NY, 1986.

[23] D. de Klerk, D, J, Rixen, J. de Jong, “The Frequency Based Substructuring (FBS) Method reformulated according to the Dual Domain Composition Method,” *Proceedings of the XXIV International Modal Analysis Conference*, 2006.

[24] M.V. van der Seijs, *Experimental Dynamic Substructuring – Analysis and Design Strategies for Vehicle Development,* Ph.D. Dissertation, KL Leuven, 2016.

[25] A.M. Steenhoek, M. W. van der Kooij, M.L.J Verhees, D.D. van den Bosch, J.M. Harvie, “Test-Based Modeling, Source Characterization and Dynamic Substructuring Techniques Applied on a Modular Industrial Demonstrator.” *Conference Proceedings of the 37$^{th}$ IMAC,* 2019.

[26] C.Q. Liu, "Combination of an Improved FRF-based Substructure Synthesis and Power Flow Method with Application to Vehicle Axle Noise Analysis." *Shock and Vibration* vol 15, no1, pp 51-60, 2008.

[27] W. Peng, "FRF-based Substructure Technique for Modeling Machinery Isolation System." *21st International Congress on Sound and Vibration 2014, ICSV 2014*, pp. 182-89.

[28] J. E. Mottershead, M. G. Tehrani, D. Stancioiu, S. James, H. Shahverdi, “Structural modification of a helicopter tailcone,” *Journal of Sound and Vibration*, Vol. 298, No. 1–2, pp. 366-384, 2006.

[29] D. Nicgorski, and P. Avitabile, "Experimental Issues Related to Frequency Response Function Measurements for Frequency-based Substructuring." *Mechanical Systems and Signal Processing* vol. 24 no. 5 pp. 1324-337, 2010.

[30] D. Nicgorski and P. Avitabile. "Conditioning of FRF Measurements for Use with Frequency Based Substructuring." *Mechanical Systems and Signal Processing* vol. 24 no. 2, pp. 340-351, 2010.

[31] D. De Klerk, D.J. Rixen, S.N. Voormeeren, and F. Pasteuning. "Solving the RDoF Problem in Experimental Dynamic Substructuring." *Proceedings of the XXVI International Modal Analysis Conference,* 2008.

[32] M. V. van der Seijs, D. D. van den Bosch, D. J. Rixen, D. de Klerk, "An Improved Methodology for the Virtual Point Transformation of Measured Frequency Response Functions in Dynamic Substructuring," *4th ECCOMAS thematic conference on computational methods in structural dynamics and earthquake engineering,* 2013, pp. 4334-4347.

[33] R. L. Mayes, E. C. Stasiunas "Lightly damped experimental substructures for combining with analytical substructures," *Proceedings of the 25$^{th}$ international modal analysis conference,* 2007